Article

Pd nanocrystals with continuously tunable high-index facets as a model nanocatalyst

Neng-Fei Yu, Na Tian, Zhi-You Zhou, Tian Sheng, Wen-Feng Lin, Jin-Yu Ye, Shuo Liu, Hai-Bin Ma, and Shi-Gang Sun

ACS Catal., **Just Accepted Manuscript** • DOI: 10.1021/acscatal.8b04741 • Publication Date (Web): 26 Feb 2019

Pd nanocrystals with continuously tunable high-index facets as a model nanocatalyst

Neng-Fei Yu[†,‡], Na Tian[‡,*], Zhi-You Zhou[‡], Tian Sheng[§], Wen-Feng Lin[ξ,*], Jin-Yu Ye[‡], Shuo Liu[‡], Hai-Bin Ma[‡] and Shi-Gang Sun[‡,*]

[†]College of Energy Science and Engineering, Nanjing Tech University, Nanjing, 211800, China.

[‡]State Key Laboratory for Physical Chemistry of Solid Surfaces Collaborative Innovation Center of Chemistry for Energy Materials College of Chemistry and Chemical Engineering Xiamen University, Xiamen, 361005, China

[ξ]Department of Chemical Engineering, Loughborough University, Loughborough, Leicestershire, LE11 3TU, UK

[§]College of Chemistry and Materials Science, Anhui Normal University, Wuhu, 241000, China.

ABSTRACT. Knowledge of the structure–reactivity relationship of catalysts is usually gained through using well-defined bulk single-crystal planes as model catalysts. However, there exists a huge gap between bulk single-crystal planes and practical nanocatalysts in terms of size, structural complexity, and local environment. Herein, we efficiently bridged this gap by developing a model nanocatalyst based on nanocrystals with continuously tunable surface structures. Pd nanocrystals with finely tunable facets, ranging from a flat {100} low-index facet

to a series of {*hk*0} high-index facets, were prepared by an electrochemical square-wave potential method. The validity of the Pd model nanocatalyst has been demonstrated by structure–reactivity studies of electrocatalytic oxidation of small organic molecules. We further observed that Pd nanocrystals exhibited catalytic performance considerably different from bulk Pd single-crystal planes with the same Miller indices. Such differences were attributed to special catalytic functions conferred by nanocrystal edges. This study paves a promising route for investigating catalytic reactions effectively at the atomic and nano- scales.

KEYWORDS. High-index facets; model catalysts; single crystalline planes; electrocatalysis; electrooxidation; structure–reactivity relationship

Graphical Abstract

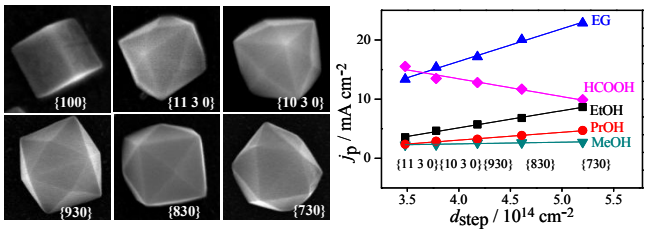

INTRODUCTION

Heterogeneous catalysis and electrocatalysis are widely applied in energy conversion and storage, oil refining and environmental decontamination.[1-2] Catalytic reactions occur only on catalyst surfaces and are thus very sensitive to the surface structure.[3-4] Understanding the structure–reactivity relationship at the atomic level is of fundamental importance for rational design of high-performance catalysts, and has long been a central concern in surface science and catalysis communities.[4-11] Practical catalysts consist of nanoparticles with abundant edge and corner sites, which typically serve as active sites.[12-15] However, practical nanocatalysts cannot be directly used for structure–reactivity studies due to their structural complexity and non-uniformity.

A strategy to overcome this hurdle is to use two-dimensional (2D) single-crystal planes with well-defined atomic arrangement as model catalysts. This strategy was originally proposed by Langmuir in 1922,[16] but only became experimentally accessible in the 1960s. As pioneers, Ertl [5] and Somorjai [17] developed model catalysts by using bulk single-crystal planes in heterogeneous catalysis, and Clavilier [18] made an initial contribution to electrocatalysis. Alternative model catalysts that consist of nanoparticles supported on single-crystal planes have also been developed for investigating support effects.[6] Although the bulk single-crystal model catalyst approach has provided valuable knowledge about surface sensitivity and active sites, etc. there exists a long-standing open question regarding a huge gap between bulk single-crystal planes and practical nanocatalysts in terms of size, structural complexity, and local environments, as illustrated in Figure 1. Bulk single-crystal planes have a macro size of millimeter scale, which is approximately six orders of magnitude larger than the nanometer size of practical catalysts, and have 2D long-range ordered surface structures. By contrast, practical nanocatalysts consist of 3D

nanoparticles with complex and irregular surface structures. Such a huge gap can lead to intrinsic differences in their catalytic behavior. For example, although bulk Au is inert for CO oxidation, Au nanoparticles smaller than 5 nm exhibit an exceptionally high activity for this reaction.[19]

To bridge this gap, new-generation model catalysts based on nanocrystals (NCs) must be developed. These NCs should have particle sizes and edge sites comparable to those of practical nanocatalysts while retain well-defined and tunable surface structures as bulk single-crystal planes (Figure 1). Clearly, the prerequisite for this approach is structure-controlled synthesis of NCs, particularly NCs with continuously tunable high-index facets (i.e., gradually tunable atomic terrace-step structures) to reveal the catalytic properties of active step/edge sites of practical nanocatalysts. To date, NCs of three low-index facets (i.e., {111}, {100}, and {110} facets) [20-23] and limited cases of high-index facets have been reported. [24-29] However, continuously tuning of high-index facets remains a challenge, which mainly arises from two aspects: (i) High-index facets have a high surface energy, which results in rapid disappearance of high-index facets during the NC growth; (ii) The Miller indices of high-index facets are continuously variable, and the difference in the surface energy of two adjacent high-index facets is very small (Figure S1 in the Supporting Information), leading to a broad distribution of the surface structures on the resultant NCs.

Tetrahexahedral (THH) Pt and Pd NCs with {730} high-index facets were firstly synthesized in our laboratory by developing an electrochemical square-wave potential (SWP) method.[24,30] The formation of high-index facets was mainly attributed to the SWP-driven repetitive adsorption/desorption of oxygen species through H_2O dissociation, which induced the formation of step sites on the surfaces through a site-exchanged mechanism.[24] A THH NC has 24 {*hk*0} high-index facets, which can be regarded as a cube with each face capped by a square-based

pyramid. The Miller indices (i.e., the values of h and k) and the density of step sites (d_{step}) can be altered theoretically by changing the geometric parameters of the THH NCs, such as the interfacial angles or the ratio of pyramid height to cube edge length (Figure S1 and Table S1 in the Supporting Information).

In this study, we synthesized a series of Pd NCs with continuously tunable surface structures ranging from {100} low-index facets to a set of {hk0} high-index facets by utilizing the electrochemical SWP method. The as-synthesized Pd NCs were served as a model nanocatalyst to study the structure–reactivity relationship at the atomic level and nanoscale, for electrocatalytic oxidation of small organic molecules relevant to direct fuel cells. Significantly different electrocatalytic behaviors towards ethanol oxidation were observed between Pd NCs and bulk Pd single-crystal planes with the same Miller indices, and correlated to the severe poisoning effect by edge sites on NCs. This study demonstrates an effective route to bridge the aforementioned gap in catalysis research between bulk single-crystal planes and practical nanocatalysts.

RESULTS AND DISCUSSION

Characterization of Pd NCs with continuously tunable facets. Figure 2A shows scanning electron microscope (SEM) and transmission electron microscope (TEM) images of the as-prepared Pd NCs with different surface structures. The overall morphology, size distribution, and surface structures are demonstrated in Figure S2-S7 in the Supporting Information. All samples had a similar average particle size of approximately 80 nm. The surface structures of the NCs were controlled by varying the upper potential (E_U) of the SWP. The higher E_U corresponds to the more intensive oxygen adsorption on the Pd surface, which facilitates the formation of more

stepped facets. As the E_U increased from 0.950 V to 1.040 V, the shapes of the Pd NCs changed from a cube of {100} facets (denoted as Cube{100}) to a series of THH of {*hk*0} high-index facets (denoted as THH{*hk*0}). To determine the Miller indices of THH Pd NCs, TEM images of Pd NCs along the [001] orientation were captured. In this orientation, eight side facets parallel to the [001] axis can be imaged edge-on and form an octagonal projection, as illustrated in Figure S1 and Figure 2A. The Miller indices were calculated according to the interfacial angle $\boldsymbol{\alpha}$ ($\boldsymbol{\alpha}$ = 2arctan(*h*/*k*)).[24, 31] For the THH NCs prepared by the SWP method with the E_U of 1.000, 1.010, 1.020, 1.030 and 1.040 V, the Miller indices varied continuously from {**11** 3 0}, {**10** 3 0}, {**9**30}, {**8**30} to {**7**30}. The surface structure of these Pd NCs was uniform. For example, TEM images of more than 20 THH{830} Pd NCs along the [001] direction were captured (Figure S8). The distribution of the interfacial angle α (four α on each NC) was very narrow with a standard deviation of around 1° (Figure 2B). This variance was essentially equal to the angle deviation of bulk single-crystal planes. Therefore, the surface structure of the as-prepared Pd NCs was adequately uniform for structure–reactivity studies. Furthermore, the high-index facets of Pd NCs were very stable in the electrochemical tests as benefited from their harsh growth conditions consisting of repeated oxidation-reduction cycling induced by the SWP. For example, both the voltammetric characteristic and the shape/Miller index of THH{830} Pd NCs changed little after subjected to 5000 potential cycles between 0.1 and 1.1 V in 0.1 M $HClO_4$ (Figure S9).

Figure 2A also illustrates the atomic arrangements of the facets of the as-prepared Pd NCs. They consisted of {100} terrace followed by {110} step periodically. Alternatively, the {730} facet can be considered as two {210} subfacets followed by one {310} subfacet periodically, and {830} facet as two {310} subfacets followed by one {210} subfacets, and {10 3 0} facet as two {310} subfacets followed by one {410} subfacets etc. The d_{step} increased in the order of {100}

<< {11 3 0} < {10 3 0} < {930} < {830} < {730} (Figure S1 and Table S1), as confirmed by the electrochemical voltammetric characterization in 0.1 M $HClO_4$ electrolyte solution (Figure 2C), where the current peaks at around 0.15 and 0.20 V were attributed to the hydrogen adsorption/desorption on Pd {110} steps and {100} terraces, respectively. [32] As expected, the former was strengthened as the Miller indices varied from {100} to {730}. Step sites are favorable for oxygen adsorption at a low potential. As a result, the integral charge of oxygen adsorption on Pd step sites from 0.70 to 0.90 V increased linearly with the calculated d_{step} on the THH NCs (Figure 2D). The surface structure of Pd NCs was further characterized by CO stripping (Figure S10). The peak potentials of CO oxidation shifted positively with increasing the d_{step}. The low-coordinated step sites facilitate the adsorption of both CO and the surface O/OH formed from water dissociative adsorption. The former is unfavorable for CO oxidation, while the latter is favorable for the oxidation reaction. The positively shifting of CO stripping peak potential with increasing step sites may indicate that the strength of the CO adsorption dominates the oxidation reaction, the latter is very sensitive to the surface structure and is consistent with the continuous change of the surface structure from {100} to {730} facets.

Structure–reactivity relationship revealed by the model nanocatalyst. The continuously tunable high-index facets of Pd NCs can be served as a model catalyst for structure–reactivity studies at nanoscale. Figure 3A illustrates voltammograms of electrocatalytic oxidation of a series of fuel cell-related small organic molecules, including formic acid, methanol, ethanol, n-propanol, and ethylene glycol. The surface-structure sensitivity is greatly different for these electrocatalytic reactions. As the d_{step} increased, the catalytic activity markedly increased for multi-carbon alcohol (ethanol, n-propanol, and ethylene glycol) oxidation, and changed little for methanol oxidation, but decreased for formic acid oxidation (Figure 3B). In addition, high-index

facets (such as THH{730}) exhibited relatively lower peak potentials for the electrooxidation of these small organic molecules in comparison to the low-index facets, which could be related to the facile formation of inert surface oxides on the highly stepped surface.[33]

To quantitatively evaluate the surface-structure sensitivity, both the peak current density (j_p) and d_{step} were normalized to the values obtained on the least stepped THH{11 3 0} Pd NCs. As shown in Figure 3C, the normalized activity ($j_{p\{hk0\}}/j_{p\{11\ 3\ 0\}}$) was linearly related to the normalized step density ($d_{step\{hk0\}}/d_{step\{11\ 3\ 0\}}$), yielding slopes of 2.93, 1.99, 1.35, 0.10, and −0.62 for the oxidation of ethanol, n-propanol, ethylene glycol, methanol, and formic acid, respectively. These slopes represented the influence of surface structure on catalytic activity. Multi-carbon alcohol oxidation exhibited a significant surface–structure sensitivity and could be ranked in order of ethanol > n-propanol > ethylene glycol, whereas methanol oxidation was generally insensitive to step sites. By contrast, formic acid oxidation demonstrated reverse surface–structure sensitivity. The negative slope indicated that the step sites were unfavorable for this reaction, which is in agreement with the previous result of bulk Pd single crystal planes reported by Hoshi and coworkers.[34]

Reaction mechanism of the electrooxidation of formic acid and ethanol. To further understand the electrooxidation mechanism, density functional theory (DFT) calculations of representative systems were carried out. According to the surface sensitivity (Figure 3C) and structure characteristics of Pd NCs (Figure 2A), the oxidation of formic acid and ethanol on the flat Pd(100) and stepped Pd(310) were modeled, and the main results are presented in Figure 4.

For formic acid oxidation, the rate determining step (RDS) was found to be the decomposition of adsorbed formate (HCOO*) via C-H bond breaking (Figure 4A). On the stepped Pd(310), the

adsorption of HCOO* is too strong for its decomposition, resulting in the step sites being poisoned by HCOO*. The barrier of C-H bond breaking is 1.04 eV on Pd(310), which is higher than the value of 0.98 eV on Pd(100). Therefore, the oxidation rate on stepped Pd(310) should be slower than that on flat Pd(100). This result is consistent with the above experimental observation that step sites are unfavorable for formic oxidation (Figure 3).

For the reaction mechanism of ethanol oxidation, adsorbed ethanol firstly breaks an α- C-H bond to form CH_3CHOH* which reacts readily with surface OH* to form acetaldehyde and water (Figure 4B). The acetaldehyde then dehydrogenates to form acetyl (CH_3CO*) rapidly, which may continue to react following two competing processes. One is the partial oxidation process where CH_3CO* is oxidized by surface OH* to form acetate, and the other is the complete oxidation process where CH_3CO* undergoes β-dehydrogenation to form CH_2CO*, the latter then further reacts involving C-C bond breaking (broken line in Figure 4B). The partial oxidation path is energetically favorable on both flat Pd(100) and stepped Pd(310) surfaces.

The RDS of partial oxidation of ethanol was found to be the cleavage of α- C-H bond to form CH_3CHOH*. This was confirmed by our previous experimental result of high H/D kinetics isotope effect (KIE=5.2) for this step.[35] On the flat Pd(100), the effective barrier of α- C-H breaking is 1.17 eV, higher than 1.12 eV on the stepped Pd(310). This is related to higher binding energy of the adsorbate on step sites. Therefore the theoretical calculations predicted that step sites are favorable for ethanol oxidation, which is in fact in line with the experimental observation (Figure 3).

Obviously the ethanol complete oxidation path is more desirable for direct ethanol fuel cell application as more electrons can be released per ethanol molecule, that is $12e^-$ in full oxidation

instead of $4e^-$ in partial oxidation. The barrier of C-C bond breaking, $CH_2CO^* \rightarrow CH_2^* + CO^*$, is 0.97 eV on the flat Pd(100), whilst it decreases to 0.77 eV on the stepped Pd(310) (Figure 4B). Therefore it is evidenced that step sites will promote the C-C bond breaking, and such increase the selectivity to the full oxidation product CO_2 from ethanol oxidation. To verify this, electrochemical *in-situ* FTIR spectra of ethanol electrooxidation at 0.8 V (near peak potential) on Pd NCs of Cube{100}, THH{310} and THH{730} were collected and shown in Figure 5. The main product detected was acetate (IR absorption at around 1415 and 1553 cm^{-1} for the symmetric and asymmetric stretching band of COO, respectively). On the other hand, the IR band intensity of CO_2 (around 2343 cm^{-1}), the full oxidation product formed through C-C bond breaking, increased significantly as Pd NCs changed from cube to THH. The ratio of the IR band intensity of CO_2 to acetate (1415 cm^{-1}), denoted as η_{CO2}, was used to evaluate the relative amount of full oxidation against the partial oxidation, i.e., the level of C-C bond breaking in the overall ethanol oxidation. The η_{CO2} obtained from the highly stepped THH{730} was 1.7 and 7.0 times higher than those from the less stepped THH{310} and the flat Cube{100}, respectively. Clearly these in-situ FTIR data is in good agreement with the DFT calculations discussed above; and confirms that the stepped sites may facilitate ethanol C-C bond dissociation.

Comparison of electrocatalytic behaviors between Pd NCs and bulk Pd single-crystal planes. Polyhedral nanocrystals have not only facets, but also edges and 3D spatial structure. Crystal edges have very low coordinated atoms, and 3D spatial structure is relevant to local mass transfer, such as diffusion field of reactants near nanocrystals. Therefore, both the edges and the 3D spatial structure are important for catalytic performance. The main advantage of the new model nanocatalyst proposed here over the traditional bulk single-crystal plane model catalysts is that the former can provide the reactivity information of edges and 3D spatial structure, relevant

to real catalyst, but the latter cannot. To demonstrate this point, we carried out comparative studies between Pd NCs and bulk Pd single-crystal planes with the same Miller indices. According to the surface structure sensitivity data shown in Figure 3C, ethanol electrooxidation on THH{310} Pd NCs and bulk Pd(310) single-crystal plane was selected as comparative study, under various ethanol concentrations and potential scan rates. Figure 6A shows cyclic voltammograms of ethanol oxidation on THH{310} Pd NCs and bulk Pd(310) single-crystal plane at 0.05 V s^{-1} in 1 M NaOH + 1 M ethanol. The catalytic activity of the bulk Pd(310) was 2.2 times higher than that of THH{310} in view of peak current density. Analogous behavior could also be observed on bulk Pd(100) plane against Cube{100} Pd NCs (Figure S11). In addition, commercial Pd black catalyst exhibited voltammetric characteristics closer to Pd NCs than bulk Pd single-crystal planes (Figure S11). When ethanol concentration decreased, the difference in catalytic activity between bulk Pd single-crystal planes and Pd NCs was enlarged sharply. For example, in 0.1 M ethanol solution, the ethanol oxidation current on Pd(310) was 19 times higher than that on THH{310} (Figure 6B). Such a big difference challenges the reliability of using bulk single-crystal planes as model catalysts to explore the catalytic behaviors of nanocatalysts.

Interestingly, it was found that the difference in catalytic activity between Pd NCs and bulk single-crystal planes was reduced as potential scan rate increased. We recorded the voltammograms in 1 M NaOH + 1 M ethanol at scan rate ranging from 0.02 to 10 V s^{-1} (Figure S12). The catalytic activity of THH{310} was close to that of Pd(310) at a very high scan rate of 10 V s^{-1} (Figure 6C). Figure 6D depicts the ratio of the forward peak current density of Pd(310) to that of THH{310} (i.e., $j_{p,Pd(310)}/j_{p,THH\{310\}}$) as a function of the potential scan rate. The initial ratio was 2.8 at a very slow scan rate of 0.02 V s^{-1}, and gradually approached to one as the scan

rate increased to 10 V s^{-1}. The similar scan rate dependence was also observed on commercial Pd black catalyst against Pd(310) (Figure S12).

THH{310} Pd NCs and bulk Pd(310) plane have the same terrace-step atoms on facets/planes, but one of the main differences is that only the former contains low-coordinated edge sites (Figure 1). The electrooxidation of small organic molecules usually involves the dissociative adsorption to generate surface CO adsorbates, which can be strongly adsorbed on the surface and poison the catalysts.[36-39] The dissociative adsorption of ethanol to form CO adsorbates involves the cleavage of strong C–H and C–C bonds, which may preferentially occur at highly active edge sites. Therefore, the electrochemical *in situ* FTIR spectra of ethanol oxidation on THH{310} and Pd(310) were collected at 0.45 V (close to the onset potential) where adsorbed CO was detected, see Figure 7A and 7B (red lines), respectively. The IR band at ~1820 cm^{-1} is assigned to bridge-bonded CO (CO_B). [37,38] To evaluate the adsorbed CO coverage, the FTIR spectra of saturated CO adsorption on the two surfaces were also collected (black lines) as references for monolayer CO adsorbates on the two surfaces. According to the relative intensity of the CO band generated from ethanol oxidation to that of the CO saturation adsorption, the CO_B coverage was estimated to be 0.088 and 0.017 for ethanol oxidation on THH{310} and Pd(310), respectively. Five times larger CO_B coverage obtained on THH{310} compared to that on Pd(310) indicates clearly that much more severe CO poisoning existed on THH{310} than that on Pd(310).

It is well known that the proportion of edge sites on the NCs increases as particle size decreases (Figure S13). To investigate the correlation between CO poisoning and the amount of edge sites, we synthesized THH{310} Pd NCs with different sizes of 39, 77, and 113 nm (Figure S13) and studied ethanol oxidation on these samples, as well as the bulk Pd(310) and the commercial Pd black. The current–time curves of ethanol oxidation at 0.65 V on these catalysts

were measured. Clearly, the decline rate of ethanol oxidation current increased with increasing the proportion of edge sites, following the order of commercial Pd black > THH{310} (39 nm) > THH{310} (77 nm) > THH{310} (113 nm) > bulk Pd(310) single-crystal plane (Figure 7C). This result suggests that the poisoning species are mainly produced on the edge sites.

The proportion of edge sites on Pd NCs is very low (< 2%). If CO species generated at edge sites were just fixed on edge sites, the catalytic activity of THH{310} should be close to that of Pd(310). This is not consistent with the experimental observation. Severe poisoning on THH{310} suggests that CO species generated at edge sites could diffuse to the facet sites, poison and deactivate them, as illustrated in Figure 7D.

The generation of CO species on edge sites may also explain the dependence of the poisoning effect on the scan rate and ethanol concentration shown in Figure 6. Generally, the dissociative adsorption of small organic molecules on noble metal surfaces to produce CO species only occurs at relatively low potentials and needs a few to tens of seconds for the accumulation of enough CO adsorbates that can poison the surfaces considerably. [36, 37] As the scan rate increased, the dwell time in the low-potential region was shortened, and the accumulated amount of CO adsorbates decreased. For example, the dwell time at low potential was only tens of milliseconds at 10 V s^{-1}, so that the accumulated CO species was negligible for such short time. Therefore, the catalytic activity of THH{310} Pd NCs trended to bulk Pd(310) as the scan rate increased (Figure 6D). The similar intrinsic activity observed on the two surfaces at a very high scan rate also supports the fact that THH{310} and Pd(310) have similar plane/facet structures. This point can help to exclude the possibility that the different catalytic activities observed in Figure 6A and 6B come from different plane/facet structures between THH{310} and Pd(310).

The ethanol concentration effect is also related to the geometrical shape that determines the local mass transfer. According to spherical diffusion model, mass transfer rate is inversely proportional to radius of curvature of a particle. Crystal edges have a small radius of curvature, and thus possess much higher mass transfer rate than facets/planes. When the ethanol concentration decreased, mass transfer became more and more dominant, and edge sites collected much more ethanol molecules than facet/plane sites. The poisoning effect on Pd NCs became more severe in low-concentration ethanol solution. It is not unreasonable to observe that the relative catalytic activity of Pd(310) against that of THH{310} increased from 2.2 to 19 when the ethanol concentration decreased from 1.0 to 0.1 M (Figure 6A and 6B).

The above results demonstrated that the catalytic activity of bulk Pd(310) was much higher than that of THH{310} for ethanol oxidation when potential scan rate or ethanol concentration decreased. This difference was attributed to the edge sites which only exist on Pd NCs. The low-coordinated edge sites promoted ethanol dissociation with C-C bond cleavage into poisoning CO adsorbates that in turn diffused to the facets and suppressed the overall catalytic activity of Pd NCs.

CONCLUSIONS

In summary, we have developed a model nanocatalyst based on well-defined surface structures of Pd nanocrystals with continuously tunable {*hk*0} high-index facets, and investigated the structure–reactivity relationship of electrooxidation of a series of small organic molecules. It has been found that Pd step sites are favorable for the oxidation of multi-carbon alcohols, but unfavorable for formic acid oxidation. Pd nanocrystals and bulk Pd single-crystal planes with the same Miller indices exhibited significantly different catalytic performance for ethanol oxidation,

depending on potential scan rate and ethanol concentration. Such a difference was attributed to the poisoning effects originating at Pd nanocrystal edge sites. The applications of this model nanocatalyst will contribute to better understanding the structure–reactivity relationship properly at the atomic and nanoscale level, and consequently to effectively realize the rational design of high-performance catalysts.

EXPERIMENTAL SECTION

Materials. Palladium dichloride ($PdCl_2$, 99.999%) and perchloric acid ($HClO_4$, super pure) were purchased from Alfa Aesar. Sodium hydroxide monohydrate ($NaOH·H_2O$, 99.9995%) was purchased from Sigma Aldrich. Methanol (MeOH), ethanol (EtOH), n-propanol (PrOH), ethylene glycol (EG) and formic acid (HCOOH) were A.R. reagents and purchased from China Medicine Shanghai Chemical Reagent Corp. The commercial Pd black catalyst was purchased from Alfa Aesar (Johnson Matthey Inc.). All chemicals were used as received. The solutions were prepared from super pure water (18 MΩ cm) purified through a Milli-Q Lab system (Millipore Ltd.)

Preparation of Pd NCs. Pd NCs were electrodeposited on a glassy carbon (GC, ϕ = 6 mm) disk electrode in 0.1 mM $PdCl_2$ + 0.1 M $HClO_4$ solution in a standard three-electrode cell at room temperature. The working electrode was the GC electrode. Prior to electrodeposition, the GC electrode was polished mechanically by successively using alumina powder of sizes 5, 1, and 0.3 μm, and cleaned in an ultrasonic bath. The counter electrode was a Pd foil and reference electrode was a saturated calomel electrode (SCE). All electrode potentials reported in this paper were quoted versus the reverse hydrogen electrode (RHE) scale. Electrode potential was controlled by PAR 263A potentiostat/galvanostat (EG&G) via a home-developed software that could realize arbitrary potential waveform. The electrochemical square-wave potential (SWP) method was applied to control the surface structure of Pd NCs. The SWP method contained the following three stages: (1) The GC electrode was first subjected to a high potential of 1.5 V (vs. RHE) and held for 4 s to clean the GC electrode; (2) The GC electrode was subjected to the potential step from 1.50 V to a low potential of 0.10 V (E_N), and held for 40 ms to generate Pd nuclei; (3) The growth of the Pd nuclei into Pd NCs was achieved by applying a SWP. The

surface structure of Pd NCs can be tuned by changing the upper potential (E_U) of SWP from 0.950 to 1.040 V. The lower potential (E_L) of SWP was 0.600 V, and the frequency (f) was 100 Hz. The growth time was 45 min.

Characterization. The morphology and structure of the as-synthesized Pd NCs were characterized by scanning electron microscopy (SEM, Hitachi S-4800) and transmission electron microscopy (TEM, JEM-2100 at 200 kV). Electrocatalytic activity of Pd nanocrystals was tested by cyclic voltammetry. Prior to the test, the cyclic voltammograms (CVs) in 0.1 M $HClO_4$ solution was firstly recorded at 0.05 V s^{-1}, and the electroactive surface area of the Pd was measured through the electric charge of hydrogen adsorption. The electrode was then transferred to the solution containing small organic molecules including formic acid (HCOOH), methanol (MeOH), ethanol (EtOH), n-propanol (PrOH), and ethylene glycol (EG), and stable CV was recorded. The solution was 0.1 M $HClO_4$ + 0.1 M HCOOH or 1.0 M NaOH + 1.0 M MeOH/EtOH/PrOH/EG. The current density was calculated through dividing the measured current by the electroactive surface area. The reproducibility of electrocatalytic tests was fairly good; for example, the relative standard deviation of peak current density recoded for ethanol electrooxidation on six samples of THH{310} Pd NCs was about 8%.

Pd single-crystal electrodes. Bulk Pd(100) and Pd(310) single-crystal planes were purchased from MaTeck GmbH. Before each measurement, the Pd single-crystal electrodes were annealed by induction heating under high-pure Ar atmosphere, and cooled also in Ar stream, and then transferred to an electrochemical cell under the protection of a droplet of super pure water. The annealed Pd single-crystal electrodes were characterized in N_2-purged 0.1 M $HClO_4$ solution by cyclic voltammetry, and then transferred to 0.1 M $HClO_4$ + 0.1 M HCOOH or 1.0 M NaOH + 1.0 M ethanol for electrocatalytic tests. The oxidation current was normalized by geometric area of the Pd electrodes to obtain the current density, since the roughness of annealed single-crystal electrodes is close to 1.

Electrochemical *in situ* infrared spectroscopy. *In situ* infrared spectroscopy was carried out using a Nexus-870 FTIR spectrometer (Nicolet) equipped with a liquid-nitrogen-cooled MCT-A detector and an EverGlo IR source. A thin-layer IR cell with a CaF_2 planar window was employed. Infrared radiation sequentially passed through the CaF_2 window and the thin-layer solution (~ 10 μm) between the window and the electrode surface, and then was reflected from

the electrode surface. The resulting spectra were reported as relative change in reflectivity, that is,

$$\frac{\Delta R}{R} = \frac{R(E_S) - R(E_R)}{R(E_R)}$$

where $R(E_S)$ and $R(E_R)$ are the single-beam spectrum collected at sample potential (E_S) and reference potential (E_R), respectively. As a result, for solution species, downward bands in the resulting spectrum indicate the formation of products, while upward bands denote the consumption of reactants. The spectral resolution was 8 cm^{-1}.

DFT computational methods. The electronic structure calculations were performed using the Vienna Ab-initio Simulation Package (VASP), using Perdew-Burke-Ernzerh (PBE) generalized gradient approximation (GGA) exchange-correlation functional. The projector-augmented-wave (PAW) pseudopotentials were utilized to describe the core electron interaction.[40-44] Considering the structure characteristics of Pd NCs, both the flat Pd(100) and stepped Pd(310) were modeled. The 4-layer close-packed Pd(100) and Pd(310) slabs were built with 24 atoms. The vacuum region layers were built more than 12 Å. The cut-off energy was 400 eV and a 3×3×1 Monkhorst-Pack *k*-point sampling was used for two-dimensional Brillouin integrations. During all the optimization processes, the bottom half atoms were fixed in the slab while the top half atoms were relaxed. The transition states were located with a constrained method with the converge criteria of the force below 0.05 eV/Å.[45] The reaction free energy (ΔG) was calculated as the $\Delta G = \Delta E - T\Delta S$, where ΔE denotes the reaction energy, and ΔS is the entropy change during the adsorption or desorption on the surface (T = 300K).

ASSOCIATED CONTENT

Supporting Information. Supplement SEM and TEM images of Pd nanocrystals and cyclic voltammograms of ethanol oxidation. This material is available free of charge via the Internet at http://pubs.acs.org.

AUTHOR INFORMATION

Corresponding Authors

* Email for N. T.: tnsd@xmu.edu.cn.

* Email for W. F. L.: w.lin@lboro.ac.uk.

* Email for S. G. S.: sgsun@xmu.edu.cn.

Notes

The authors declare no competing financial interest.

ACKNOWLEDGMENT

This work was supported by grants from National Key Research and Development Program of China (2017YFA0206500), Natural Science Foundation of China (21603103, 91645121, and 21621091), the UK EPSRC (EP/I013229/1) and Natural Science Foundation Committee of Jiangsu Province (BK20171462). We thank Prof. N. Hoshi from Chiba University, Prof. Y. Y. Tong from Georgetown University, Prof. Z. Q. Tian, Z. X. Xie, N. F. Zheng and L. S. Zheng from Xiamen University for fruitful discussion, and X. Lin from the Department of Chemical Engineering and Biotechnology, University of Cambridge for proof reading.

REFERENCES

(1) Somorjai, G. A.; Frei, H.; Park, J. Y. Advancing the Frontiers in Nanocatalysis, Biointerfaces, and Renewable Energy Conversion by Innovations of Surface Techniques. *J. Am. Chem. Soc.* **2009**, *131*, 16589-16605.
(2) Chen, C.; Kang, Y.; Huo, Z.; Zhu, Z.; Huang, W.; Xin, H. L.; Snyder, J. D.; Li, D.; Herron, J. A.; Mavrikakis, M.; Chi, M.; More, K. L.; Li, Y.; Markovic, N. M.; Somorjai, G. A.; Yang, P.; Stamenkovic, V. R. Highly Crystalline Multimetallic Nanoframes with Three-Dimensional Electrocatalytic Surfaces. *Science* **2014**, *343*, 1339-1343.
(3) Shuai, D.; McCalman, D. C.; Choe, J. K.; Shapley, J. R.; Schneider, W. F.; Werth, C. J. Structure Sensitivity Study of Waterborne Contaminant Hydrogenation Using Shape- and Size-Controlled Pd Nanoparticles. *ACS Catal.* **2013**, *3*, 453-463.
(4) Van Santen, R. A. Complementary Structure Sensitive and Insensitive Catalytic Relationships. *Acc. Chem. Res.* **2009**, *42*, 57-66.
(5) Ertl, G. Reactions at Surfaces: From Atoms to Complexity (Nobel lecture). *Angew. Chem. Int. Ed.* **2008**, *47*, 3524-3535.

(6) Schauermann, S.; Freund, H. J. Model Approach in Heterogeneous Catalysis: Kinetics and Thermodynamics of Surface Reactions. *Acc. Chem. Res.* **2015**, *48*, 2775-2782.
(7) Huang, W. Oxide Nanocrystal Model Catalysts. *Acc. Chem. Res.* **2016**, *49*, 520-527.
(8) Seh, Z. W.; Kibsgaard, J.; Dickens, C. F.; Chorkendorff, I.; Nørskov, J. K.; Jaramillo, T. F. Combining Theory and Experiment in Electrocatalysis: Insights into Materials Design. *Science* **2017**, *355*, 146. (and eaad4998).
(9) Zhang, G. R.; Zhao, D.; Feng, Y. Y.; Zhang, B.; Su, D. S.; Liu, G.; Xu, B. Q. Catalytic Pt-on-Au Nanostructures: Why Pt Becomes More Active on Smaller Au Particles. *ACS Nano* **2012**, *6*, 2226-2236.
(10) Kuzume, A.; Herrero, E.; Feliu, J. M. Oxygen Reduction on Stepped Platinum Surfaces in Acidic Media. *J. Electroanal. Chem.* **2007**, *599*, 333-343.
(11) Attard, G. A. Electrochemical Studies of Enantioselectivity at Chiral Metal Surfaces. *J. Phys. Chem. B* **2001**, *105*, 3158-3167.
(12) Gontard, L. C.; Chang, L. Y.; Hetherington, C. J. D.; Kirkland, A. I.; Ozkaya, D.; Dunin-Borkowski, R. E. Aberration-Corrected Imaging of Active Sites on Industrial Catalyst Nanoparticles. *Angew. Chem. Int. Ed.* **2007**, *46*, 3683-3685.
(13) Wu, C. Y.; Wolf, W. J.; Levartovsky, Y.; Bechtel, H. A.; Martin, M. C.; Toste, F. D.; Gross, E. High-Spatial-Resolution Mapping of Catalytic Reactions on Single Particles. *Nature* **2017**, *541*, 511-515.
(14) Luo, M. C.; Sun, Y. J.; Zhang, X.; Qin, Y. N.; Li, M. Q.; Li, Y. J.; Li, C. J.; Yang, Y.; Wang, L.; Gao, P.; Lu, G.; Guo, S. J. Stable High-Index Faceted Pt Skin on Zigzag-Like PtFe Nanowires Enhances Oxygen Reduction Catalysis. *Adv. Mater.* **2018**, *30*, 1705515.
(15) Huang, X.; Zhao, Z.; Cao, L.; Chen, Y.; Zhu, E.; Lin, Z.; Li, M.; Yan, A.; Zettl, A.; Wang, Y. M.; Duan, X.; Mueller, T.; Huang, Y. High-Performance Transition Metal-Doped Pt_3Ni Octahedra for Oxygen Reduction Reaction. *Science* **2015**, *348*, 1230-1234.
(16) Langmuir, I. Part II. "Heterogeneous reactions". Chemical Reactions on Surfaces. *Trans. Faraday Soc.* **1922**, *17*, 607-620.
(17) Somorjai, G. A. *Chemistry in Two Dimensions: Surfaces*; Cornell University Press: Ithaca, 1981.
(18) Clavilier, J.; Faure, R.; Guinet, G.; Durand, R. Preparation of Mono-Crystalline Pt Microelectrodes and Electrochemical Study of the Plane Surfaces Cut in the Direction of the (111) and (110) Planes. *J. Electroanal. Chem.* **1980**, *107*, 205-209.
(19) Haruta, M.; Kobayashi, T.; Sano, H.; Yamada , N. Novel Gold Catalysts for the Oxidation of Carbon-Monoxide at a Temperature Far Below 0-degrees-C. *Chem. Lett.* **1987**, *16*, 405-408.
(20) Ahmadi, T. S.; Wang, Z. L.; Green, T. C.; Henglein, A.; ElSayed, M. A. Shape-Controlled Synthesis of Colloidal Platinum Nanoparticles. *Science* **1996**, *272*, 1924-1926.
(21) Sun, Y.; Xia, Y. Shape-Controlled Synthesis of Gold and Silver Nanoparticles. *Science* **2002**, *298*, 2176-2179.
(22) Xia, Y.; Xiong, Y.; Lim, B.; Skrabalak, S. E. Shape-Controlled Synthesis of Metal Nanocrystals: Simple Chemistry Meets Complex Physics? *Angew. Chem. Int. Ed.* **2009**, *48*, 60-103.
(23) Niu, W.; Zhang, L.; Xu, G. Shape-Controlled Synthesis of Single-Crystalline Palladium Nanocrystals. *ACS Nano* **2010**, *4*, 1987-1996.

(24) Tian, N.; Zhou, Z. Y.; Sun, S. G.; Ding, Y.; Wang, Z. L. Synthesis of Tetrahexahedral Platinum Nanocrystals with High-Index Facets and High Electro-oxidation Activity. *Science* **2007**, *316*, 732-735.
(25) Zhou, Z. Y.; Tian, N.; Li, J. T.; Broadwell, I.; Sun, S. G. Nanomaterials of High Surface Energy with Exceptional Properties in Catalysis and Energy Storage. *Chem. Soc. Rev.* **2011**, *40*, 4167-4185.
(26) Zhang, J. A.; Langille, M. R.; Personick, M. L.; Zhang, K.; Li, S. Y.; Mirkin, C. A. Concave Cubic Gold Nanocrystals with High-Index Facets. *J. Am. Chem. Soc.* **2010**, *132*, 14012-14014.
(27) Quan, Z.; Wang, Y.; Fang, J. High-Index Faceted Noble Metal Nanocrystals. *Acc. Chem. Res.* **2013**, *46*, 191-202.
(28) Lin, H. X.; Lei, Z. C.; Jiang, Z. Y.; Hou, C. P.; Liu, D. Y.; Xu, M. M.; Tian, Z. Q.; Xie, Z. X. Supersaturation-Dependent Surface Structure Evolution: From Ionic, Molecular to Metallic Micro/Nanocrystals. *J. Am. Chem. Soc.* **2013**, *135*, 9311-9314.
(29) Niu, W. X.; Duan, Y. K.; Qing, Z. K.; Huang, H. J.; Lu, X. M. Shaping Gold Nanocrystals in Dimethyl Sulfoxide: Toward Trapezohedral and Bipyramidal Nanocrystals Enclosed by {311} Facets. *J. Am. Chem. Soc.* **2017**, *139*, 5817-5826.
(30) Tian, N.; Zhou, Z. Y.; Yu, N. F.; Wang, L. Y.; Sun, S. G. Direct Electrodeposition of Tetrahexahedral Pd Nanocrystals with High-Index Facets and High Catalytic Activity for Ethanol Electrooxidation. *J. Am. Chem. Soc.* **2010**, *132*, 7580-7581.
(31) Tian, N.; Zhou, Z. Y.; Sun, S. G. Platinum Metal Catalysts of High-Index Surfaces: From Single-Crystal Planes to Electrochemically Shape-Controlled Nanoparticles. *J. Phys. Chem. C* **2008**, *112*, 19801-19817.
(32) Zhang, H. X.; Wang, H.; Re, Y. S.; Cai, W. B. Palladium Nanocrystals Bound by {110} or {100} Facets: from one Pot Synthesis to Electrochemistry. *Chem. Commun.* **2012**, *48*, 8362-8364.
(33) Li, N. H.; Sun, S. G.; Chen S. P. Studies on the Role of Oxidation States of the Platinum Surface in Electrocatalytic Oxidation of Small Primary Alcohols. *J. Electroanal. Chem.* **1997**, *430*, 57-67.
(34) Hoshi, N.; Nakamura, M.; Kida, K. Structural Effects on the Oxidation of Formic Acid on the High Index Planes of Palladium. *Electrochem. Commun.* **2007**, *9*, 279-282.
(35) Ren, J.; Yang, Y. Y.; Zhang, B. W.; Tian, N.; Cai, W. B.; Zhou, Z. Y.; Sun, S. G. H-D kinetic isotope effects of alcohol electrooxidation on Au, Pd and Pt electrodes in alkaline solutions. *Electrochem. Commun.* **2013**, *37*, 49-52.
(36) Del Colle, V.; Berna, A.; Tremiliosi-Filho, G.; Herrero, E.; Feliu, J. M. Ethanol Electrooxidation onto Stepped Surfaces Modified by Ru Deposition: Electrochemical and Spectroscopic Studies. *Phys. Chem. Chem. Phys.* **2008**, *10*, 3766-3773.
(37) Yang, Y. Y.; Ren, J.; Li, Q. X.; Zhou, Z. Y.; Sun, S. G.; Cai, W. B. Electrocatalysis of Ethanol on a Pd Electrode in Alkaline Media: An in Situ Attenuated Total Reflection Surface-Enhanced Infrared Absorption Spectroscopy Study. *ACS Catal.* **2014**, *4*, 798-803.
(38) Zhou, Z. Y.; Wang, Q.; Lin, J. L.; Tian, N.; Sun, S. G. In situ FTIR Spectroscopic Studies of Electrooxidation of Ethanol on Pd Electrode in Alkaline Media. *Electrochim. Acta* **2010**, *55*, 7995-7999.
(39) Sun, S. G.; Clavilier, J. Electrochemical Study on the Poisoning Intermediate Formed from Methanol Dissociation at Low Index and Stepped Platinum Surfaces. *J. Electroanal. Chem.* **1987**, *236*, 95-112.

(40) Kresse, G.; Hafner, J. Ab Initio Molecular Dynamics for Open-Shell Transition Metals. *Phys. Rev. B* **1993**, *48*, 13115-13118.
(41) Kresse, G.; Furthmuler, J. Efficient Iterative Schemes for Ab Initio Total-Energy Calculations Using a Plane-Wave Basis Set. *Phys. Rev. B* **1996**, *54*, 11169-11186.
(42) Blochl, P. E. Projector Augmented-Wave Method. *Phys. Rev. B* **1994**, *50*, 17953-17979.
(43) Kresse, G.; Joubert, D. From Ultrasoft Pseudopotentials to the Projector Augmented-Wave Method. *Phys. Rev. B* **1999**, *59*, 1758-1775.
(44) Pedrew, J. P.; Burke, K.; Ernzerhof, M. Generalized Gradient Approximation Made Simple. *Phys. Rev. Lett.* **1996**, *77*, 3865-3868.
(45) Alavi, A.; Hu, P.; Deutsch, T.; Silvestrelli, P. L.; Hutter, J. CO Oxidation on Pt(111): An Ab Initio Density Functional Theory Study. *Phys. Rev. Lett.* **1998**, *80*, 3650-3653.

Figures

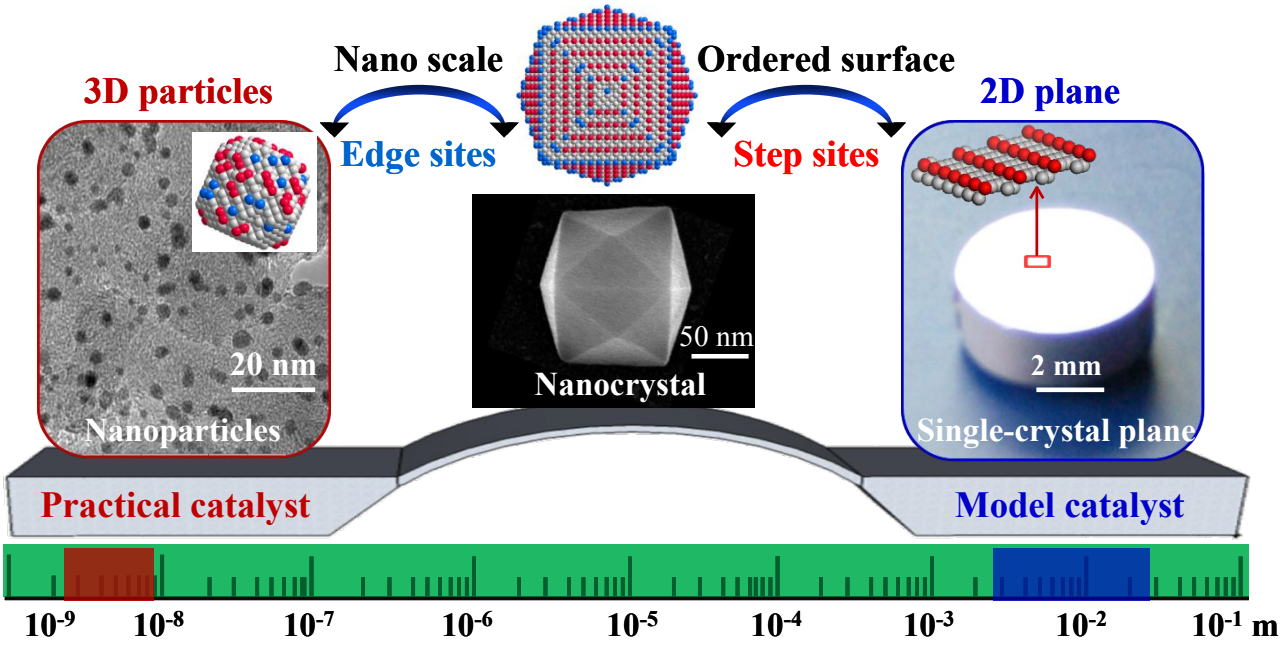

Figure 1. Illustration of the principle of continuously tunable nanocrystals to bridge the gap between model catalysts of single-crystal planes and practical catalysts. Practical catalysts consist of 3D nanoparticles with complex surface structures, whilst traditional model catalysts are macro-sized 2D single-crystal planes with ordered structure. Nanocrystals synthesized in this study have tunable and ordered facets as single-crystal planes, and edge sites as those on practical catalysts, thus they can serve as a new model catalyst to bridge the gap between model catalysts of single-crystal planes and practical catalysts.

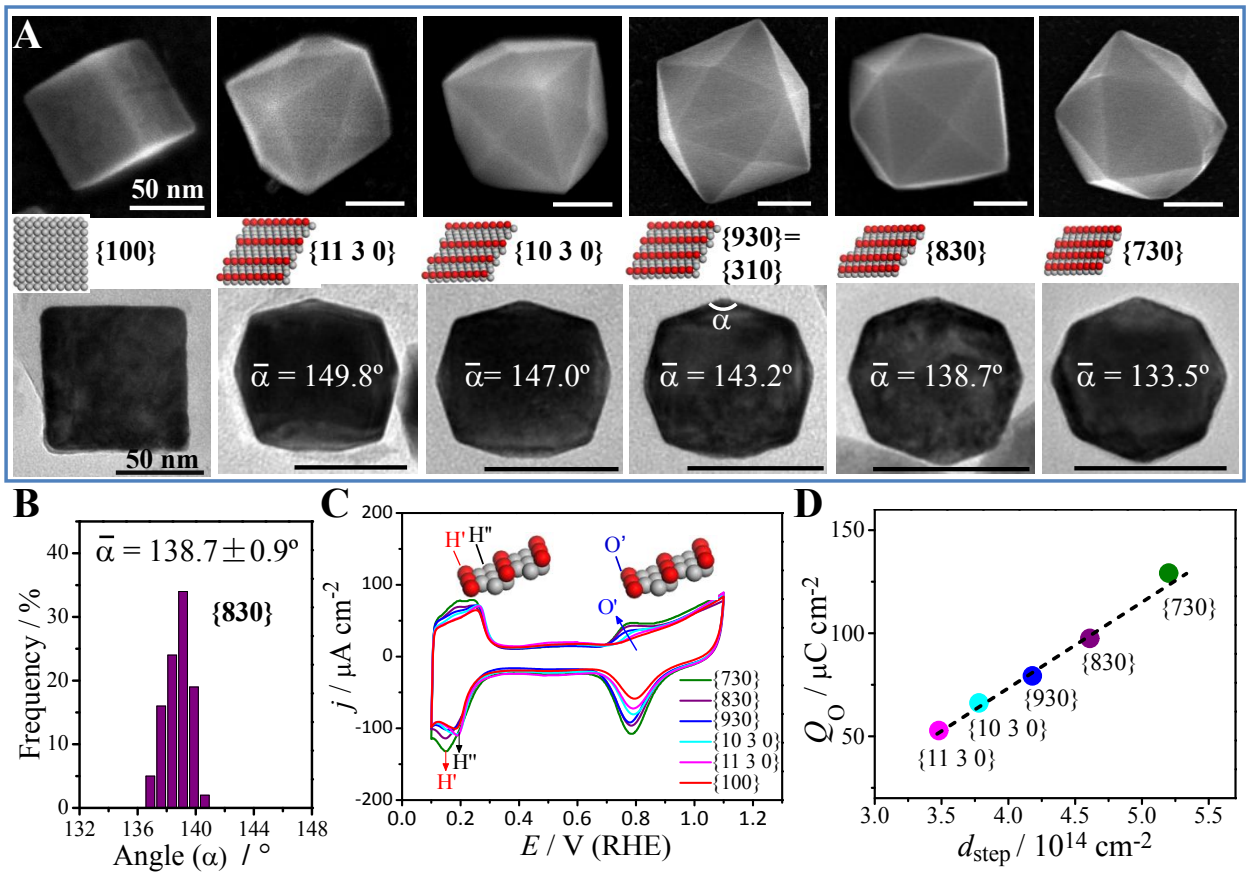

Figure 2. (A) SEM and TEM images of Pd NCs prepared by electrochemical square-wave potential method with different upper limit potential (E_U) in 0.1 mM $PdCl_2$ + 0.1 M $HClO_4$. The scale bars represent 50 nm. Pd nanocubes were obtained at E_U = 0.950 V; THH Pd NCs with {11 3 0}, {10 3 0}, {930}, {830} and {730} facets were obtained at E_U of 1.000, 1.010, 1.020, 1.030 and 1.040 V, respectively. The atomic models of these facets are also illustrated. (B) Histogram of the interfacial angle α of THH{830} Pd NCs. (C) Cyclic voltammograms of the Pd NCs recorded in 0.1 M $HClO_4$ solution, scan rate: 0.05 V s^{-1}. (D) Integral charge density (Q_O) associated with oxygen-species adsorption on the step sites of THH Pd NCs between 0.700 to 0.900 V as a function of the calculated density of step sites.

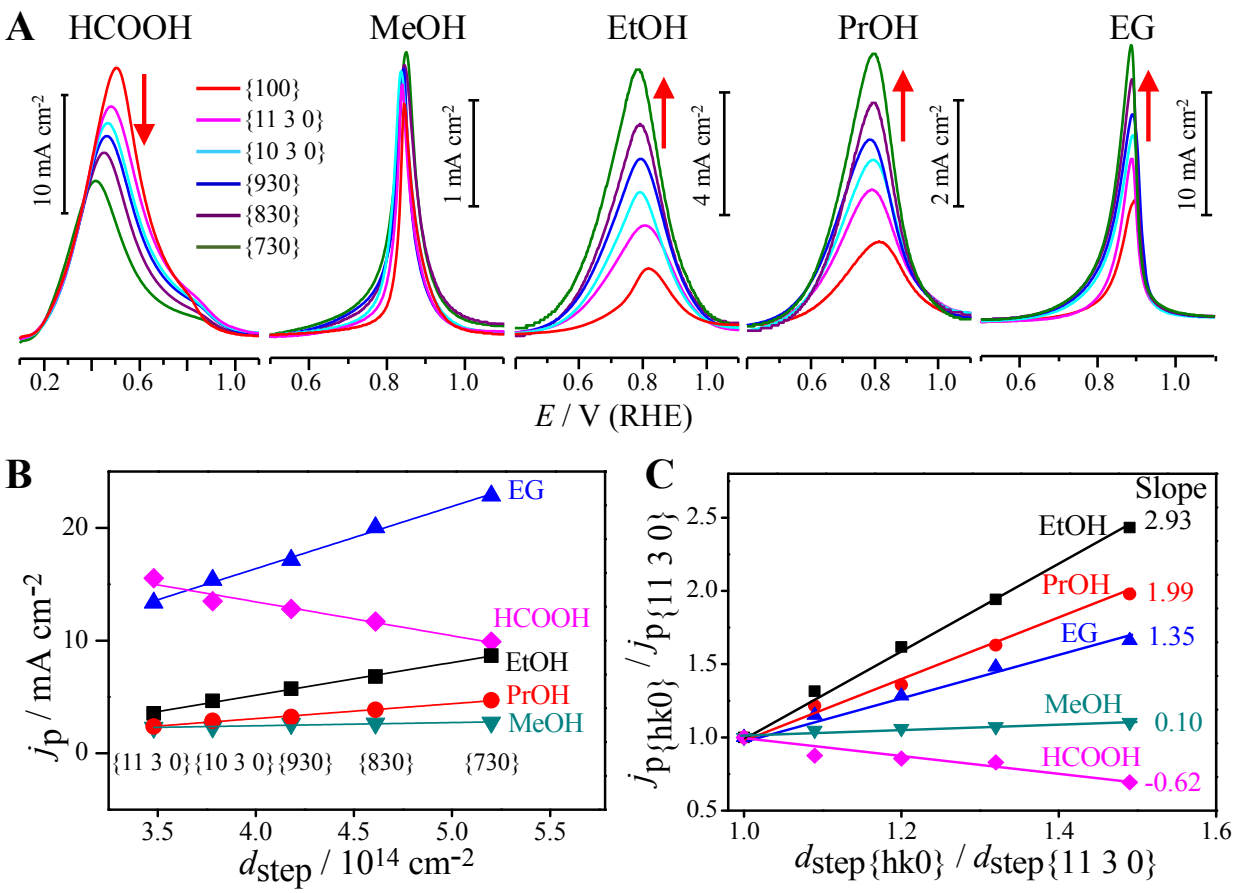

Figure 3. (A) Linear sweep voltammograms of electrooxidation of formic acid (HCOOH), methanol (MeOH), ethanol (EtOH), n-propanol (PrOH), and ethylene glycol (EG) on the Pd NCs. The solution was 0.1 M $HClO_4$ + 0.1 M HCOOH or 1.0 M NaOH + 1.0 M MeOH/EtOH/PrOH/EG. Scan rate: 0.05 V s^{-1}. (B) The dependence of peak current density on the density of step sites. (C) Normalized peak current density *vs.* normalized density of step sites using the values of THH{11 3 0} as reference. The slopes reflect the surface-structure sensitivity of the reactions.

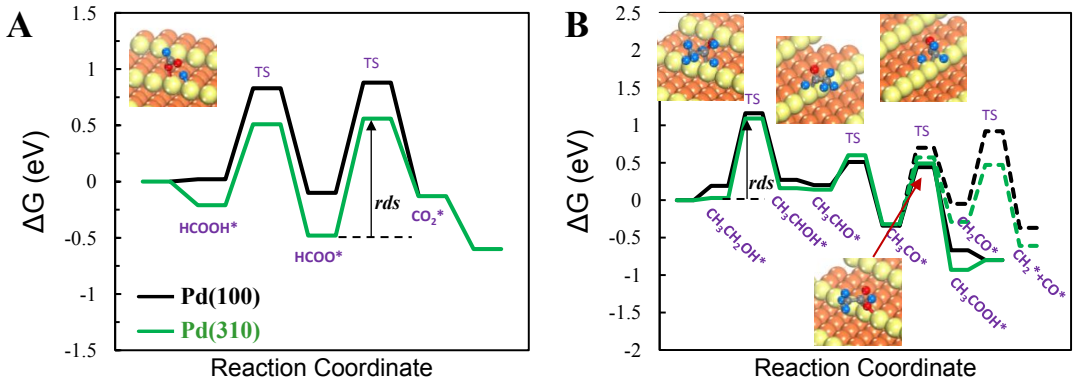

Figure 4. Free energy profiles for the oxidation of formic acid (A) and ethanol (B) on the flat Pd(100) and stepped Pd(310) planes. Black line is for Pd(100) plane and green line for Pd(310) plane. The broken line in (B) is for the complete oxidative reaction process of ethanol involving the C-C bond breaking. Insets are the key located transition states on Pd(310). Brown and yellow balls represent Pd on terrace and step sites, respectively; blue balls: H; grey balls: C; red balls: O.

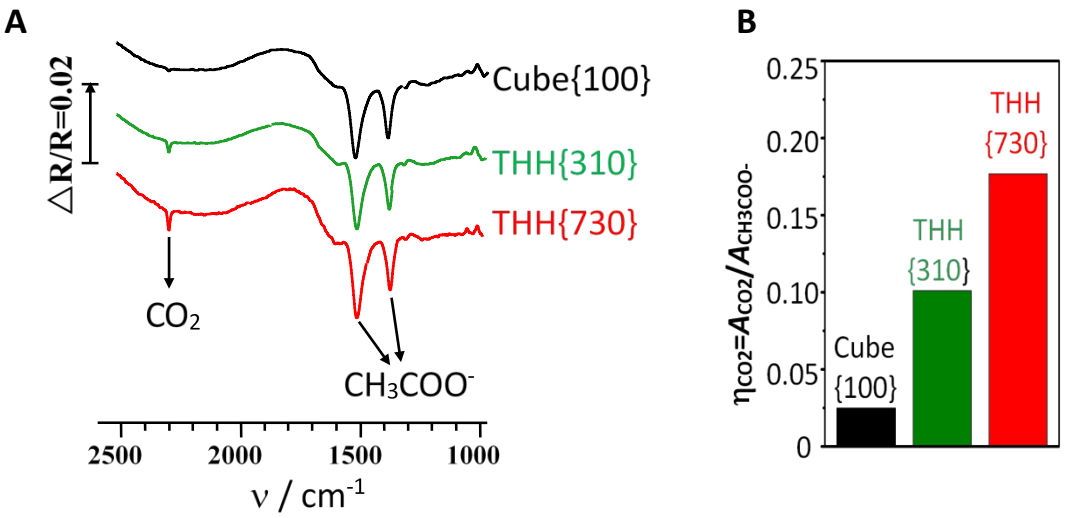

Figure 5. (A) *In situ* FTIR spectra of ethanol oxidation on Pd NCs of Cube{100}, THH{310}, and THH{730} in 1.0 M ethanol + 0.1 M NaOH solution. Sample potential E_S = 0.8 V; reference potential E_R = 0.1 V. (B) The ratio of IR band intensities (peak area) of CO_2 at around 2343 cm^{-1} to acetate at around 1415 cm^{-1}.

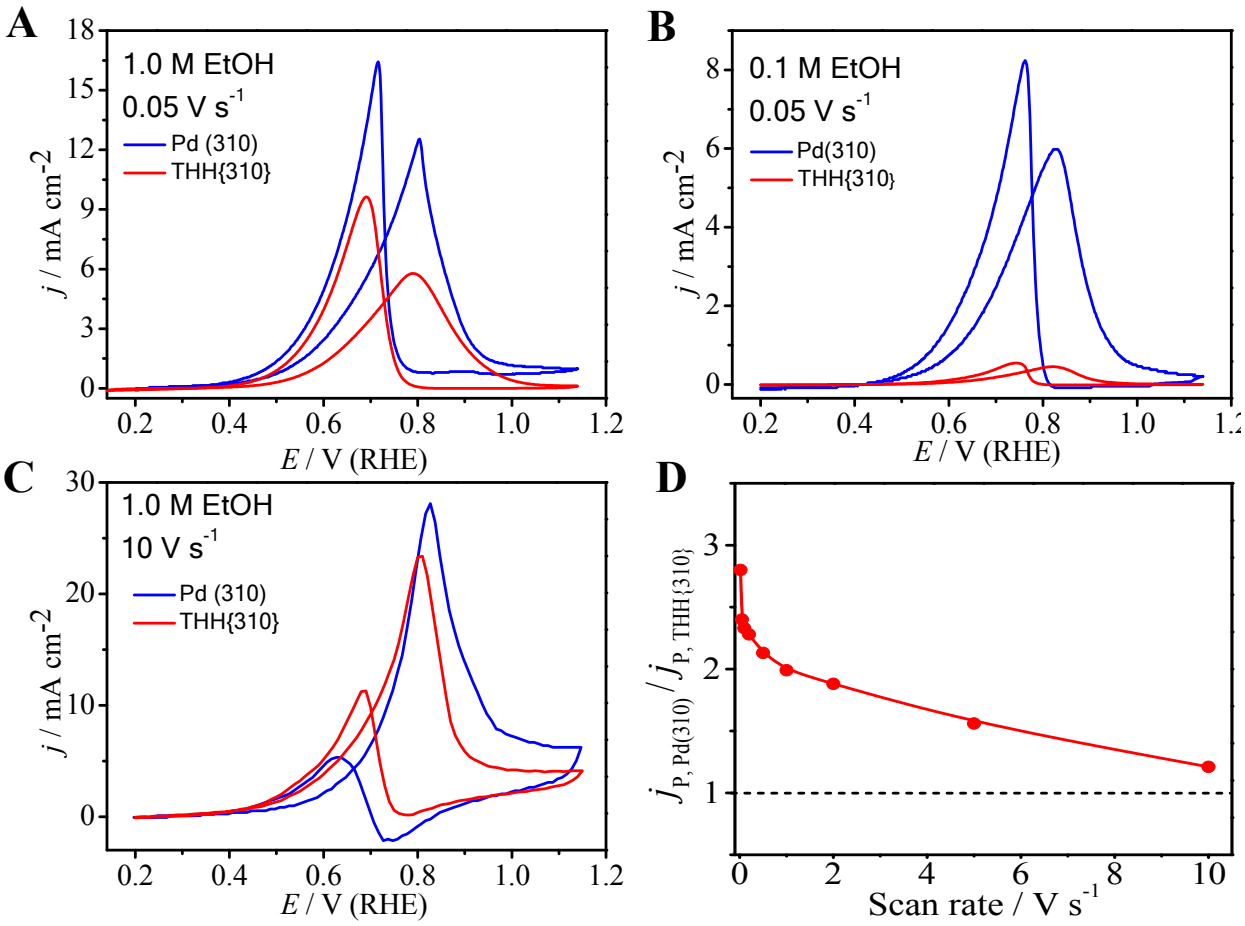

Figure 6. Cyclic voltammograms of ethanol electrooxidation on THH{310} and Pd(310) in (A) 1.0 M ethanol + 1.0 M NaOH at 0.05 V s^{-1}; (B) 0.1 M ethanol + 1.0 M NaOH at 0.05 V s^{-1}; (C) 1.0 M ethanol + 1.0 M NaOH at 10 V s^{-1}. (D) The ratio of the forward peak current density of ethanol oxidation on Pd(310) to that on THH{310} as a function of potential scan rate varying from 0.02 to 10 V s^{-1}, same ethanol solution as in (C).

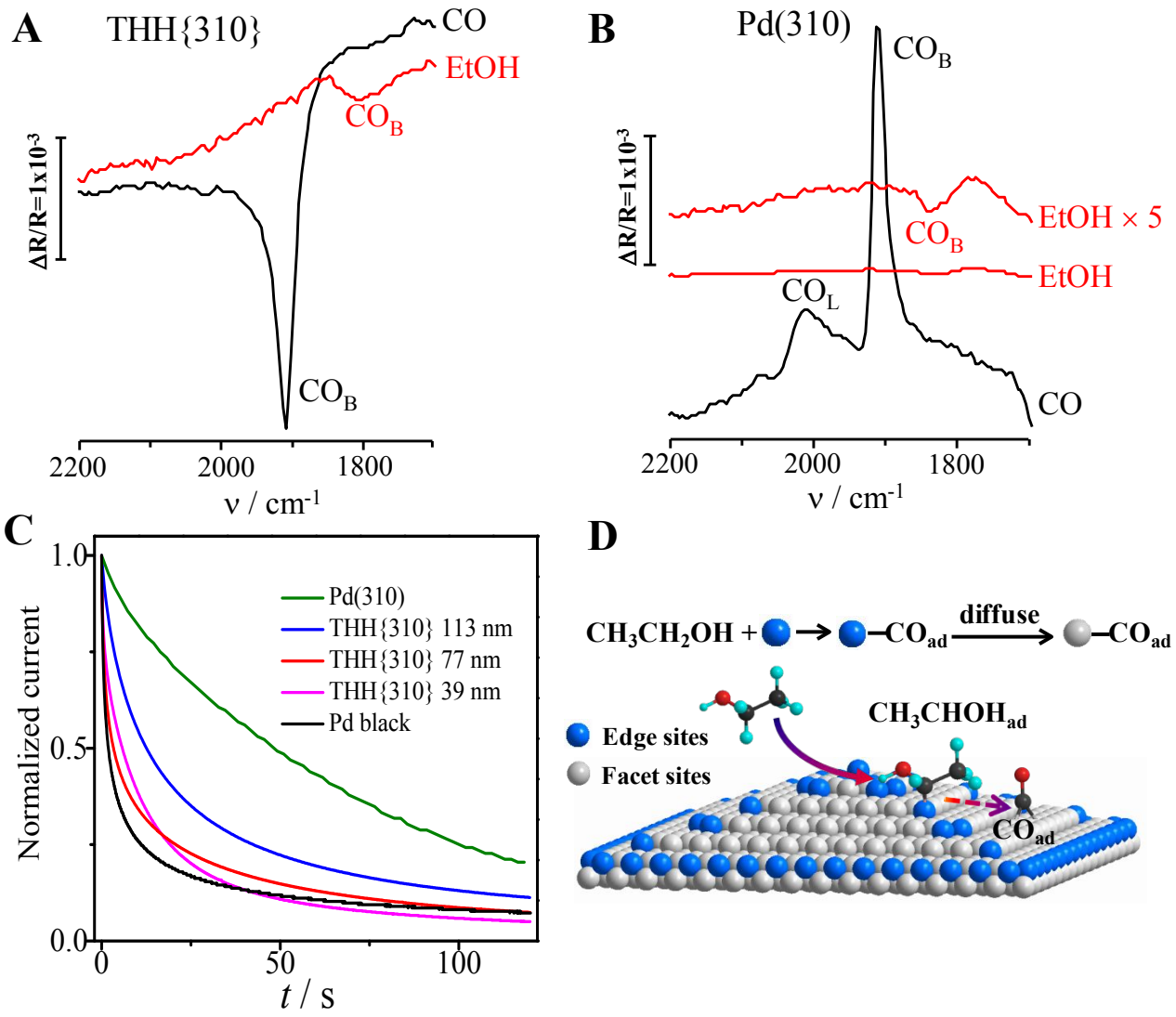

Figure 7. (A, B) Electrochemical *in situ* FTIR spectra of the CO adsorbates generated from the dissociative adsorption of ethanol (red lines) on THH{310} Pd NCs (A) and bulk Pd(310) surface (B) in 1 M NaOH + 1 M ethanol (sample potential E_S = 0.45 V, reference potential E_R = 0.25 V) and the saturated monolayer CO adsorbate (black lines) in 1 M NaOH (E_S = 0.85 V, E_R = 0.25 V). The spectrum of the CO generated from ethanol on bulk Pd(310) enlarged by 5 times was also shown in B for clarity. (C) Normalized current–time curves for ethanol oxidation on THH{310} Pd NCs of different sizes, bulk Pd(310), and commercial Pd black catalyst at 0.65 V in 1.0 M ethanol + 1.0 M NaOH. (D) Illustration of CO poisoning effect of THH Pd NCs. Edge sites promote ethanol dissociation to produce poisoning CO adsorbates that diffuse to the facets and deactivate them.

Supporting Information for

Pd nanocrystals with continuously tunable high-index facets as a model nanocatalyst

Neng-Fei Yu[†,‡], Na Tian[‡,*], Zhi-You Zhou[‡], Tian Sheng[§], Wen-Feng Lin[ξ,*], Jin-Yu Ye[‡], Shuo Liu[‡], Hai-Bin Ma[‡] and Shi-Gang Sun[‡,*]

[†]College of Energy Science and Engineering, Nanjing Tech University, Nanjing, 211800, China.

[‡]State Key Laboratory for Physical Chemistry of Solid Surfaces Collaborative, Innovation Center of Chemistry for Energy Materials, College of Chemistry and Chemical Engineering, Xiamen University, Xiamen, 361005, China

[ξ]Department of Chemical Engineering, Loughborough University, Loughborough, Leicestershire, LE11 3TU, UK

[§]College of Chemistry and Materials Science, Anhui Normal University, Wuhu, 241000, China.

1. Analysis of surface structure of tetrahexahedral Pd nanocrystals (THH Pd NCs)

A tetrahexahedron can be seen as a cube with each face capped by a square-based pyramid, and has 24 {*hk*0} high-index facets. The Miller indices of the facets on a THH NC of face-centered cubic metals depend on its geometric parameters, such as the interfacial angle (***α***) or the ratio of the height of square-based pyramid to the edge length of cube (***b/a***), as illustrated in Figure S1. The facets are best revealed by imaging the THH NC along [001], parallel to which 8 of the 24 facets are observed edge-on. The Miller indices can be determined through measuring the interfacial angles ***α***.

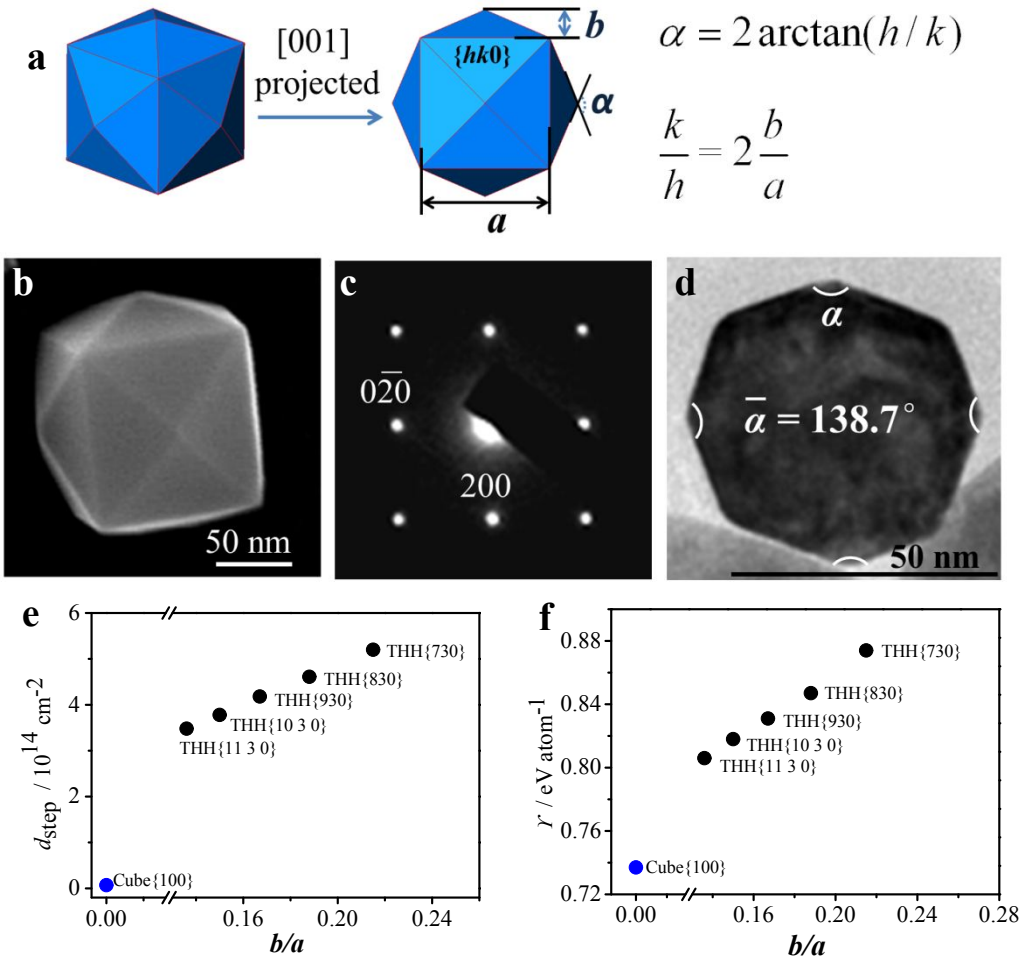

Figure S1. (**a**) Model of THH NC viewed from near [111] direction and [001] direction. (**b**) SEM image of a THH Pd NC. (**c**) Selected–area electron diffraction (SAED) pattern of a THH Pd NC along [001] direction. (**d**) TEM image of the THH Pd NC recorded along [001] direction. (**e**) Variation of the density of step sites against the structure parameter of ***b/a*** of THH Pd NCs. (**f**) Variation of the surface energy against ***b/a***.

The interfacial angle ***α*** was measured to be 138.7°, which is close to the theoretical value of 138.9° on a THH NC enclosed by {830} facets (see table S1).

When the geometric parameters (such as angle ***α*** and the value of ***b/a***) of THH Pd NCs change, the Miller indices of facets, the density of step sites (d_{step}) and the surface energy will vary accordingly, as listed in Table S1. That is, the surface structure of THH Pd NCs is adjustable. As illustrated in Figure S1e and S1f, the d_{step} and surface energy approximately increase linearly with the value of ***b/a*** in the Miller indices ranging from {11 3 0} to {730}. It is well known that the surface energy plays a key role in surface structure-controlled synthesis of metal NCs, because NCs growth tends to the lowest total surface energy. Clearly, THH Pd NCs enclosed by {*hk*0} high-index facets possess much higher surface energy than the cubic Pd NCs bounded with {100) facets. In addition, the difference in surface energy of vicinal {*hk*0} high-index facets is very small, only about 10 milli-eV atom^{-1} (Table S1). Such a small difference in the energy level leads to a great difficulty in achieving continuously tunable {*hk*0} high-index facets of THH Pd NCs.

Table S1. Theoretical values of the interfacial angle (***α***), the ratio of the height of square-based pyramid to the edge length of cube (***b/a***), Miller indices, the density of step sites (d_{step}) and the surface energy of different {*hk*0} facets on THH Pd NCs.

α	***b/a***	**Miller indices**	d_{step} **/ 10^{14} cm^{-2}**	**Surface energy / eV atom^{-1}**
/	0	{100}	/	0.737
149.5°	0.136	{11 3 0}	3.48	0.806
146.6°	0.150	{10 3 0}	3.78	0.818
143.1°	0.167	{930}={310}	4.18	0.831
138.9°	0.188	{830}	4.61	0.847
133.6°	0.214	{730}	5.20	0.874

2. Characterization of Pd NCs with continuously tunable surface structures

2.1 Pd nanocubes enclosed by {100} facets (Cube {100})

Pd nanocubes of {100} facets were obtained at E_U = 0.950 V. Figure S2 shows the SEM and TEM characterizations of them. Statistical analysis indicates that the yield of cubic morphology of Pd NCs reaches as high as 90%, and the average size of the Pd nanocubes is 76 ± 12 nm.

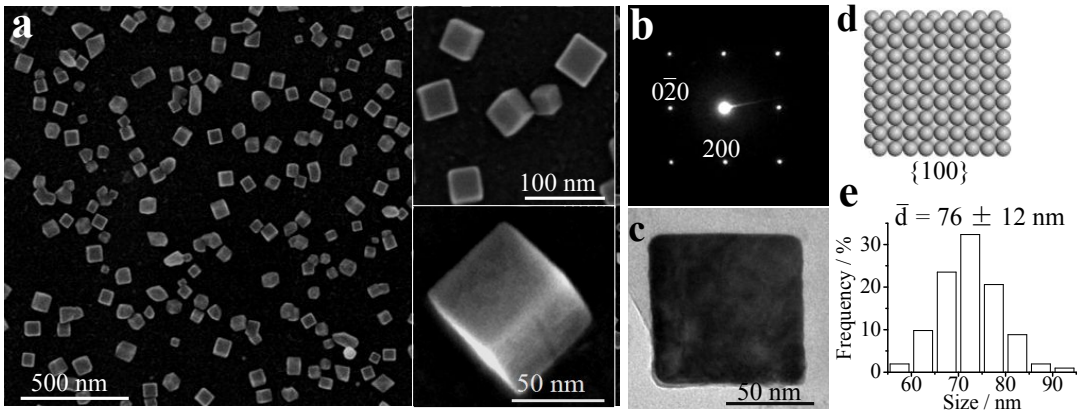

Figure S2. Morphology and structure characterization of Pd nanocubes. The electrochemical synthesis was conducted at E_N = 0.100 V, t_N = 0.04 s, E_L = 0.600 V, E_U = 0.950 V, f = 100 Hz, and with growth time t_{growth} = 45 min, in 0.1 mM $PdCl_2$ + 0.1 M $HClO_4$ solution. (**a**) SEM image of Pd nanocubes, the insets are the high-magnification SEM images of the Pd nanocubes; (**b**) SAED pattern of a Pd nanocube along [001] direction; (**c**) TEM image of the Pd nanocube along [001] direction; (**d**) Model of atomic arranged of {100} facets; (**e**) Histogram of size distribution of the Pd nanocubes.

2.2 THH Pd NCs enclosed by {11 3 0} facets (THH{11 3 0})

THH Pd NCs of {11 3 0} facets were obtained at E_U = 1.000 V. Figure S3 shows the SEM and TEM characterizations of them. Statistical analysis indicates that the yield of THH morphology of Pd NCs exceeds 90%, and the average size is 80 ± 14 nm. The average value of interfacial angle α on the THH Pd NCs is measured to be 149.9°, which is very close to the theoretical value of α = 149.5° on a THH NC enclosed by {11 3 0} facets. The atomic arrangement of the Pd{11 3 0} surface is periodically composed of two {410} subfacets followed by one {310} subfacet, and the density of step sites is 3.48×10^{14} cm^{-2}.

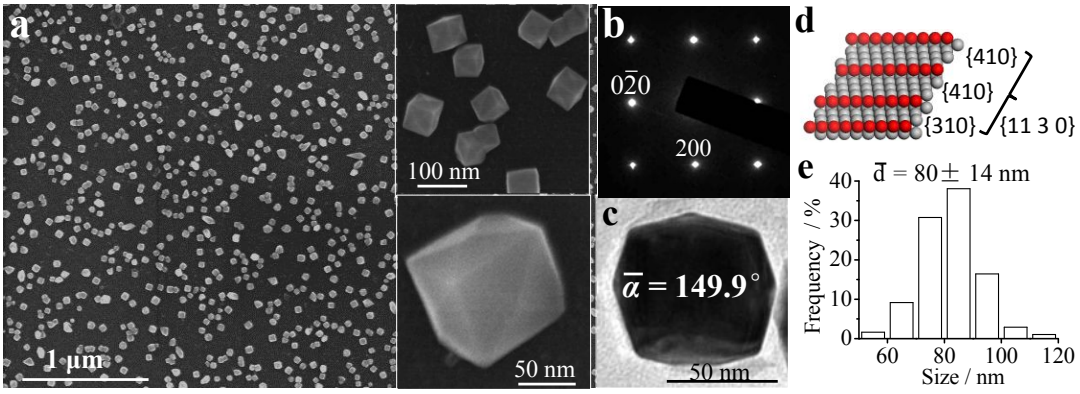

Figure S3. Morphology and structure characterization of THH{11 3 0} Pd NCs. The electrochemical synthesis was conducted at E_N = 0.100 V, t_N = 0.04 s, E_L = 0.600 V, E_U = 1.000 V, f = 100 Hz, and with growth time t_{growth} = 45 min, in 0.1 mM $PdCl_2$ + 0.1 M $HClO_4$ solution. (a) SEM image of THH Pd NCs, the insets are the high-magnification SEM images of the THH Pd NCs; (b) SAED pattern of a THH Pd NC along [001] direction; (c) TEM image of the THH Pd NC along [001] direction; (d) Model of atomic arrangement of {11 3 0} plane; (e) Histogram of size distribution of the THH{11 3 0}.

2.3 THH Pd NCs enclosed by {10 3 0} facets (THH{10 3 0})

THH Pd NCs of {10 3 0} facets were obtained at E_U = 1.010 V. Figure S4 shows the SEM and TEM characterizations of them. The average size is 79 ± 15 nm. The average value of interfacial angle α on the THH Pd NCs is measured to be 147.0°, which is close to the theoretical value of α = 146.6° on a THH NC enclosed by {10 3 0} facets. The atomic arrangement of the Pd{10 3 0} surface is periodically composed of two {310} subfacets followed by one {410} subfacet, and the density of step sites is 3.78×10^{14} cm^{-2}.

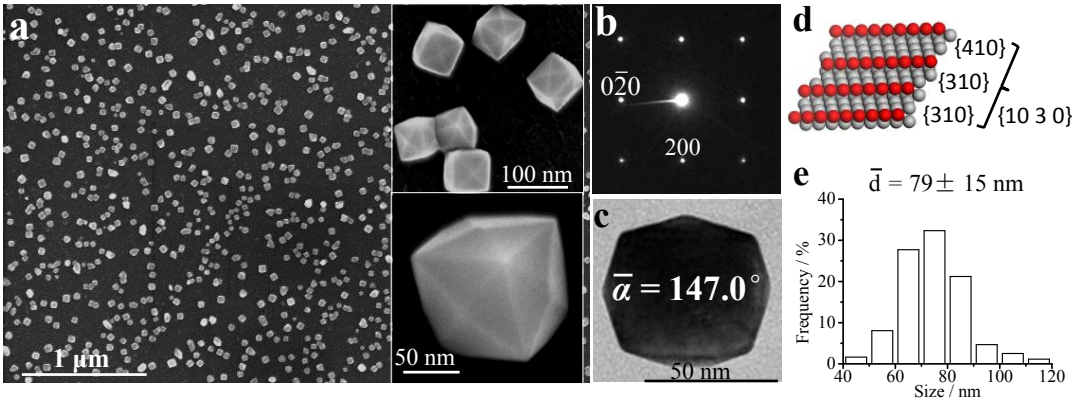

Figure S4. Morphology and structure characterization of THH{10 3 0} Pd NCs. The electrochemical synthesis was conducted at E_N = 0.100 V, t_N = 0.04 s, E_L = 0.600 V, E_U = 1.010 V, f = 100 Hz, and with growth time t_{growth} = 45 min, in 0.1 mM $PdCl_2$ + 0.1 M $HClO_4$ solution. (**a**) SEM image of THH Pd NCs, the insets are the high-magnification SEM images of the THH Pd NCs; (**b**) SAED pattern recorded by rotating the THH Pd NC to [001] direction; (**c**) TEM image of the THH Pd NC along [001] direction; (**d**) Model of atomic arrangement of {10 3 0} plane; (**e**) Histogram of size distribution of the THH{10 3 0}.

2.4 THH Pd NCs enclosed by {930} facets (THH{930})

The {930} facet is equal to {310} facet. THH Pd NCs of {930} facets were obtained at E_U = 1.020 V. Figure S5 shows the SEM and TEM characterizations of them. The average size is 77 ± 14 nm. The average value of interfacial angle α on the THH Pd NCs is measured to be 143.2°, which is very close to the theoretical value of α = 143.1° on a THH NC enclosed by {930} facets. The density of step sites on {930} is 4.18×10^{14} cm^{-2}.

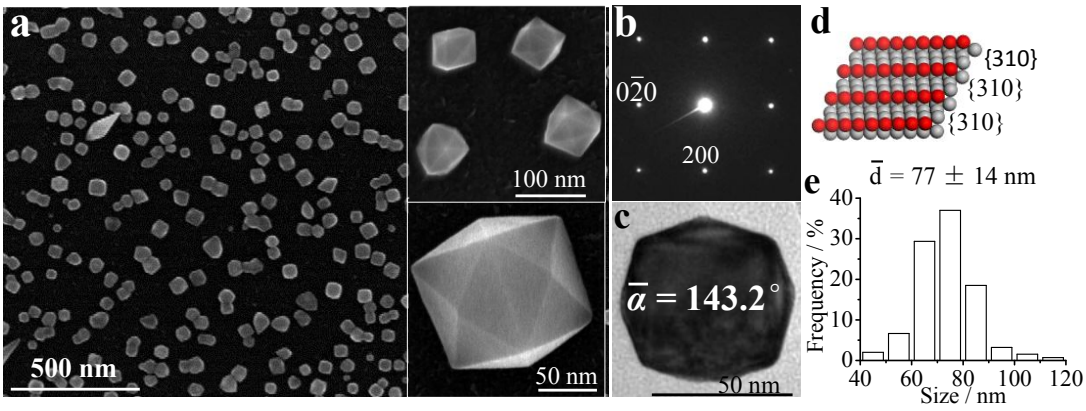

Figure S5. Morphology and structure characterization of THH{930} Pd NCs. The electrochemical synthesis was conducted at E_N = 0.100 V, t_N = 0.04 s, E_L = 0.600 V, E_U = 1.020 V, f = 100 Hz, and with growth time t_{growth} = 45 min, in 0.1 mM $PdCl_2$ + 0.1 M $HClO_4$ solution. (**a**) SEM image of THH Pd NCs, the insets are the high-magnification SEM images of the THH Pd NCs; (**b**) SAED pattern recorded by rotating the THH Pd NC to [001] direction; (**c**) TEM image of the THH Pd NC along [001] direction; (**d**) Model of atomic arrangement of {930} plane; (**e**) Histogram of size distribution of the THH{930}.

2.5 THH Pd NCs enclosed by {830} facets (THH{830})

THH Pd NCs of {830} facets were obtained at E_U = 1.030 V. Figure S6 shows the SEM and TEM characterizations of them. The average size is 76 ± 15 nm. The average value of interfacial angle α on the THH Pd NCs is measured to be 138.7°, which is close to the theoretical value of α = 138.9° on a THH NC enclosed by {830} facets. The atomic arrangement of the Pd {830} surface is periodically composed of two {310} subfacets followed by one {210} subfacet, and the density of step sites is 4.61×10^{14} cm^{-2}.

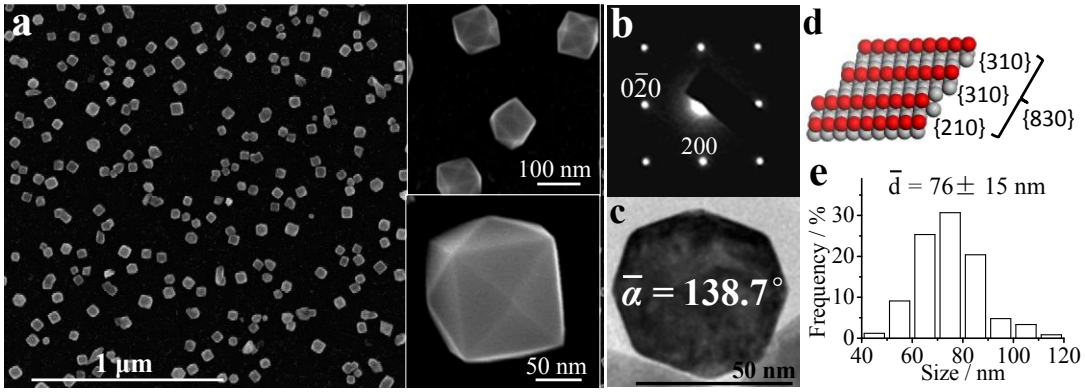

Figure S6. Morphology and structure characterization of THH{830} Pd NCs. The electrochemical synthesis was conducted at E_N = 0.100 V, t_N = 0.04 s, E_L = 0.600 V, E_U = 1.030 V, f = 100 Hz, t_{growth} = 45 min, and in 0.1 mM $PdCl_2$ + 0.1 M $HClO_4$ solution. (**a**) SEM images of THH Pd NCs, the insets are the high-magnification SEM images of the THH Pd NCs; (**b**) SAED pattern recorded by rotating the THH Pd NC to [001] direction; (**c**) TEM image recorded with the THH Pd NC along [001] direction; (**d**) Model of atomic arrangement of {830} plane; (**e**) Histogram of size distribution of the THH{830}.

2.6 THH Pd NCs enclosed by {730} facets (THH{730})

THH Pd NCs of {730} facets were obtained at E_U = 1.040 V. Figure S7 shows the SEM and TEM characterizations of them. The average size is 78 ± 15 nm. The average value of interfacial angle α on the THH Pd NCs is measured to be 133.6°, which is very close to the theoretical value of α = 133.6° on a THH NC enclosed by {730} facets. The atomic arrangement of the Pd{730} surface is periodically composed of two {210} subfacets followed by one {310} subfacet, and the density of step sites is 5.20×10^{14} cm^{-2}.

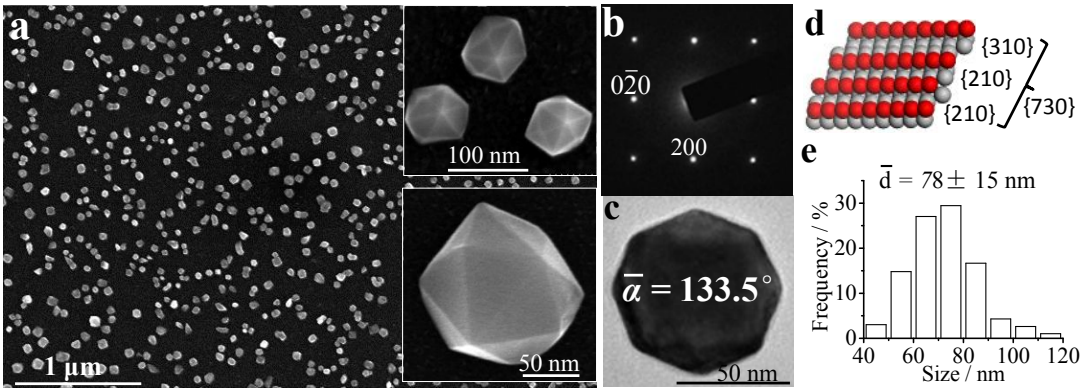

Figure S7. Morphology and structure characterization of THH{730} Pd NCs. The electrochemical synthesis was conducted at E_N = 0.100 V, t_N = 0.04 s, E_L = 0.600 V, E_U = 1.040 V, f = 100 Hz, and with growth time t_{growth} = 45 min, in 0.1 mM $PdCl_2$ + 0.1 M $HClO_4$ solution. (**a**) SEM image of THH Pd NCs, the insets are the high-magnification SEM images of the THH Pd NCs; (**b**) SAED pattern recorded by rotating the THH Pd NC to [001] direction; (**c**) TEM image of the THH Pd NC along [001] direction; (**d**) Model of atomic arrangement of {730} plane; (**e**) Histogram of size distribution of the THH{730}.

2.7 The distribution of interfacial angle (α) of THH Pd NCs

To reveal the uniformity of the facets, we captured TEM images of over 20 THH Pd NCs along [001] direction and measured the interfacial angle of **α**. Figure S8 shows the TEM images of {830}-faceted THH Pd NCs. The result indicates that the average value of interfacial angle **α** is 138.7°, and the deviation is as small as 0.9°, which is essentially the same with the angle deviation (about ± 1°) of bulk single-crystal planes during the orientation and cutting.

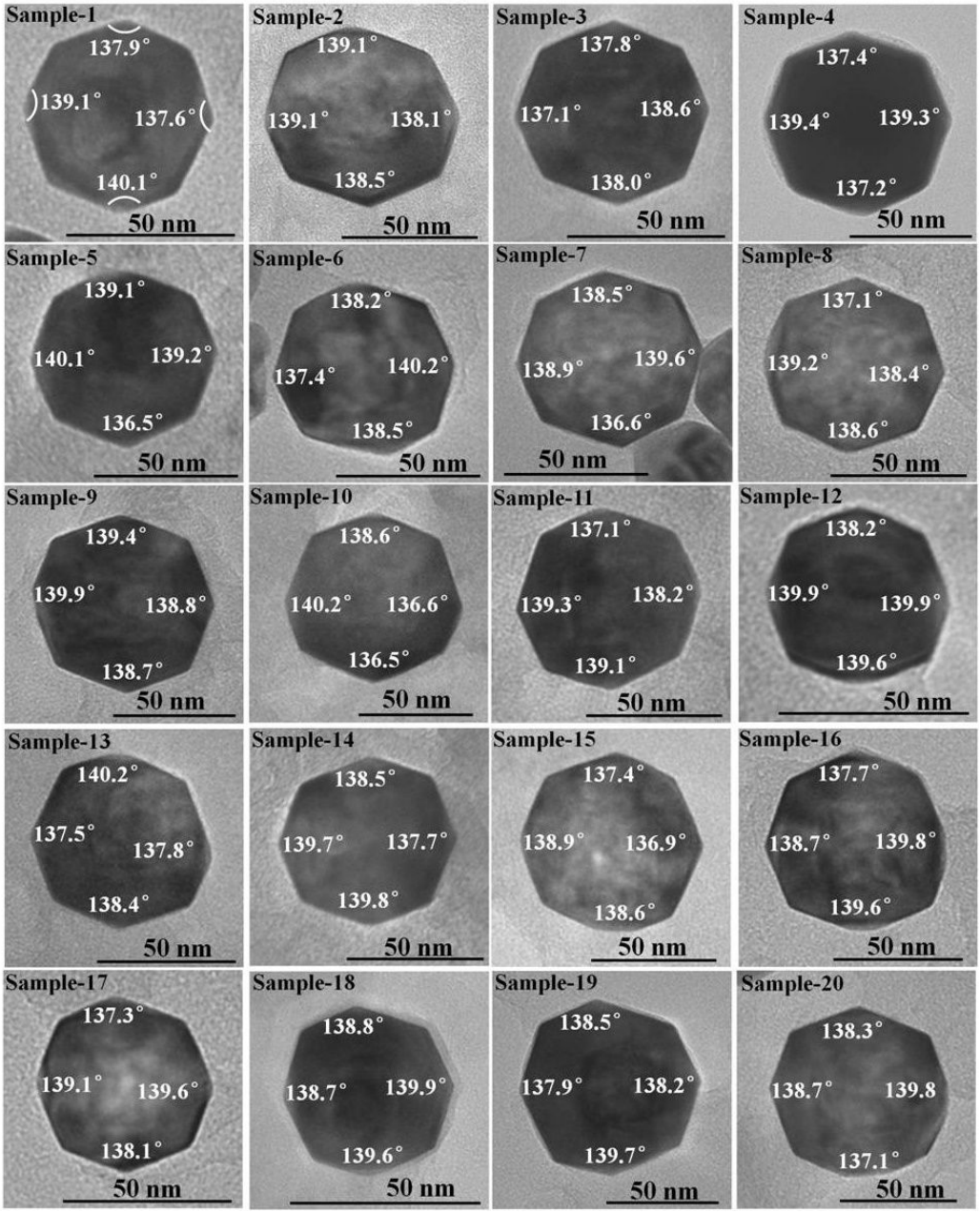

Figure S8. Some representative TEM images of THH{830} Pd NCs for the statistics of the distribution of interfacial angle α. All TEM images of the THH Pd NCs were recorded along [001] direction.

3. Electrochemical stability of Pd NCs with high-index facets

High-index facets were formed under the very harsh electrochemical conditions consisting of repeated oxidation–reduction cycling induced by square-wave potential, so it is expected that THH Pd NCs have high resistance against electrochemical corrosion. To verify it, we carried out a stability test of THH{830} Pd NCs by applying 5000 potential cycles between 0.1 and 1.1 V (vs RHE) at 0.05 V s^{-1} in 0.1 M $HClO_4$. As shown in Figure S9, the cyclic voltammogram of THH{830} changed little after the 5000 potential cycles. The peak current of hydrogen and oxygen adsorption/desorption only decreased by 0.4% and 0.2%, respectively, after the 5000 potential cycles. Moreover, the SEM and TEM data shows that Pd NCs still maintained perfect THH shape with the {830} surface facet after the stability test. The interfacial angle (α) was very close to the theoretical of 138.9° for {830}-faceted THH NC. These experimental results demonstrated that the surface structure of THH Pd NCs was very stable under applied potential at the normal electrochemical conditions.

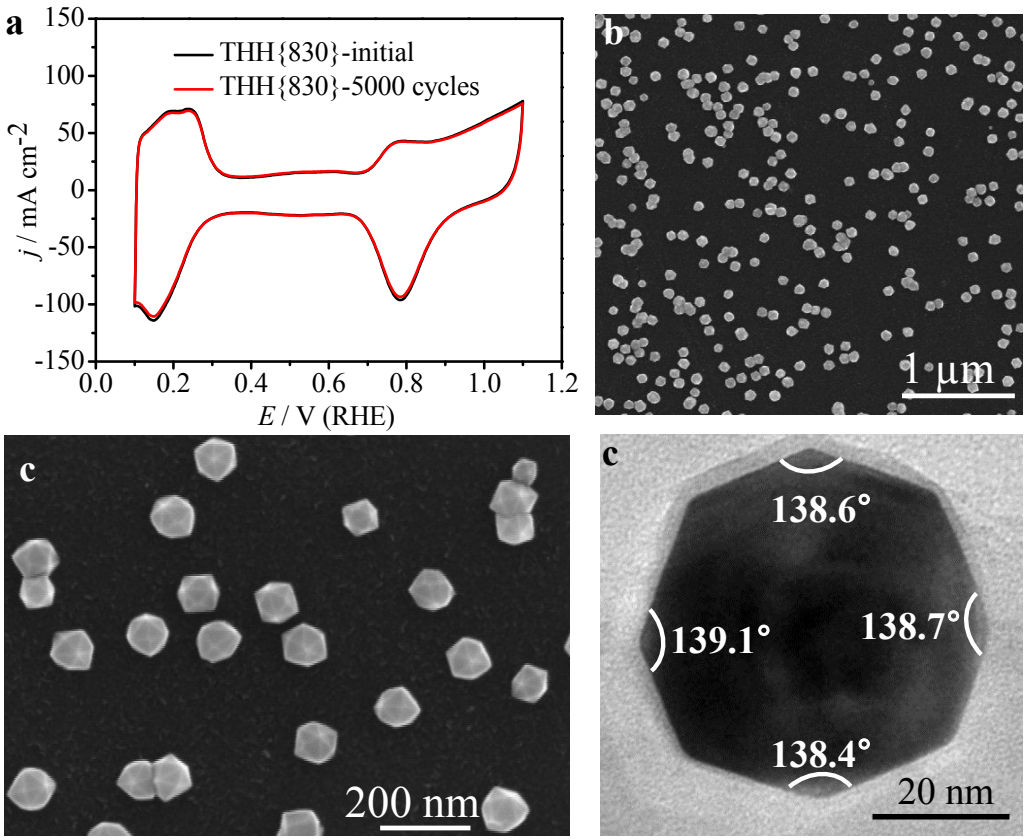

Figure S9. (a) Cyclic voltammograms of THH{830} Pd NCs in 0.1 M $HClO_4$ before and after a stability test by applying 5000 potential cycles between 0.1 and 1.1 V (vs RHE) at 0.05 V s^{-1}. (b, c) Low- and high-magnification SEM and (d) TEM images of THH{830} Pd NCs after the stability test.

4. CO stripping on Pd NCs

CO is widely used as a probe molecule to study surface structure and properties. We tested the CO stripping on the Pd NCs with different crystal faces, as shown in the Figure S10. The peak potentials of CO oxidation shifted positively with increasing the density of step sites (d_{step}). The low-coordinated step sites may facilitate the adsorption of both CO and the surface O/OH formed from water dissociative adsorption. The former is unfavorable for CO oxidation, while the latter is favorable for the oxidation reaction. The positively shifting of CO stripping peak potential with increasing step sites may indicate that the strength of the CO adsorption dominates the oxidation reaction, the latter is very sensitive to the surface structure and is consistent with the continuous change of the surface structure from {100} to {730} facets. Such relationship between CO stripping peak potential and the density of step sites also confirms the variation of surface structure of Pd NCs.

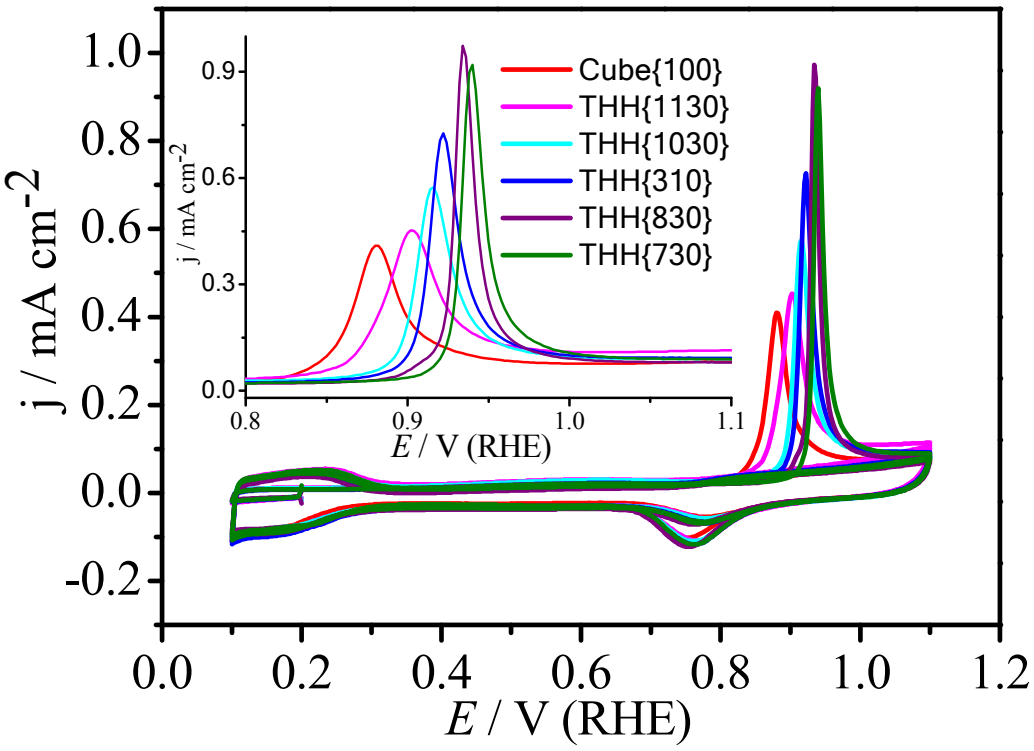

Figure S10. CO stripping voltammograms recorded on a series of Pd NCs in 0.1M $HClO_4$ solution. Scan rate: 0.05 V s^{-1}. CO was pre-adsorbed at the lower potential region then the solution CO was removed by N_2 purge for 20 min before the stripping tests. The inset shows the magnified voltammograms near the oxidation peak potential.

5. Electrochemical behaviors of Pd catalysts

5.1 Comparison of catalytic activity of different Pd catalysts for ethanol oxidation

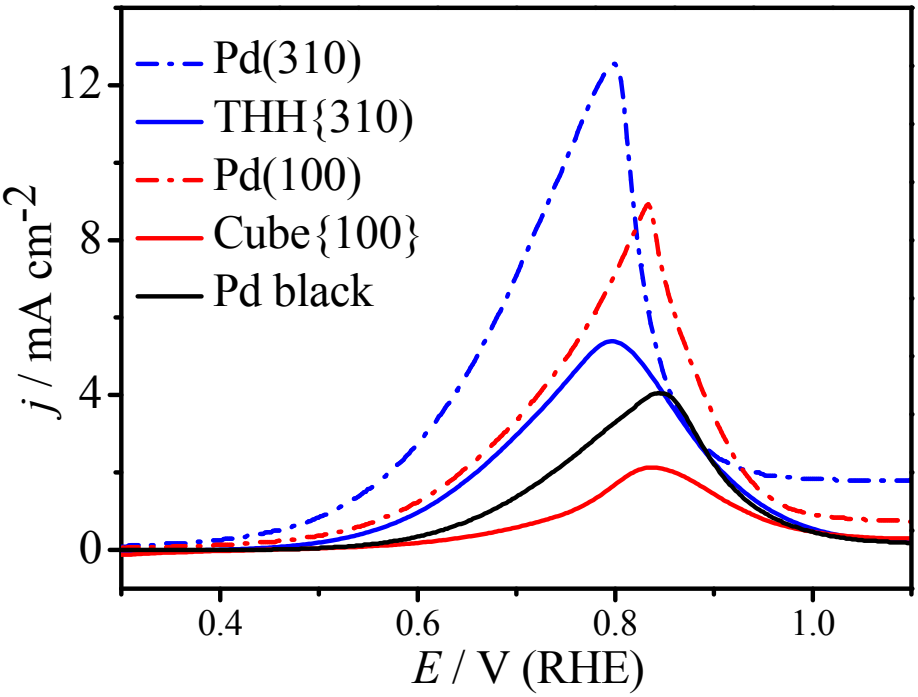

Figure S11. Comparison of voltammograms of ethanol electrooxidation on bulk Pd(310) and Pd(100) planes, Pd NCs of THH{310} and Cube{100}, as well as a commercial Pd black catalyst. The solution: 1.0 M CH_3CH_2OH + 1.0 M NaOH; scan rate: 0.05 V s^{-1}.

5.2 Dependence of scan rate on the electrocatalytic activity of different Pd catalysts

Figure S12 illustrates the CVs of ethanol oxidation on Pd(310), THH{310}, and commercial Pd black at different scan rates ranging from 0.02 to 10 V s^{-1}. At low scan rate (< 1 V s^{-1}), the j_p of Pd(310) is much larger than those of THH{310} and Pd black. At high scan rate, the j_p on different catalysts tends to similar.

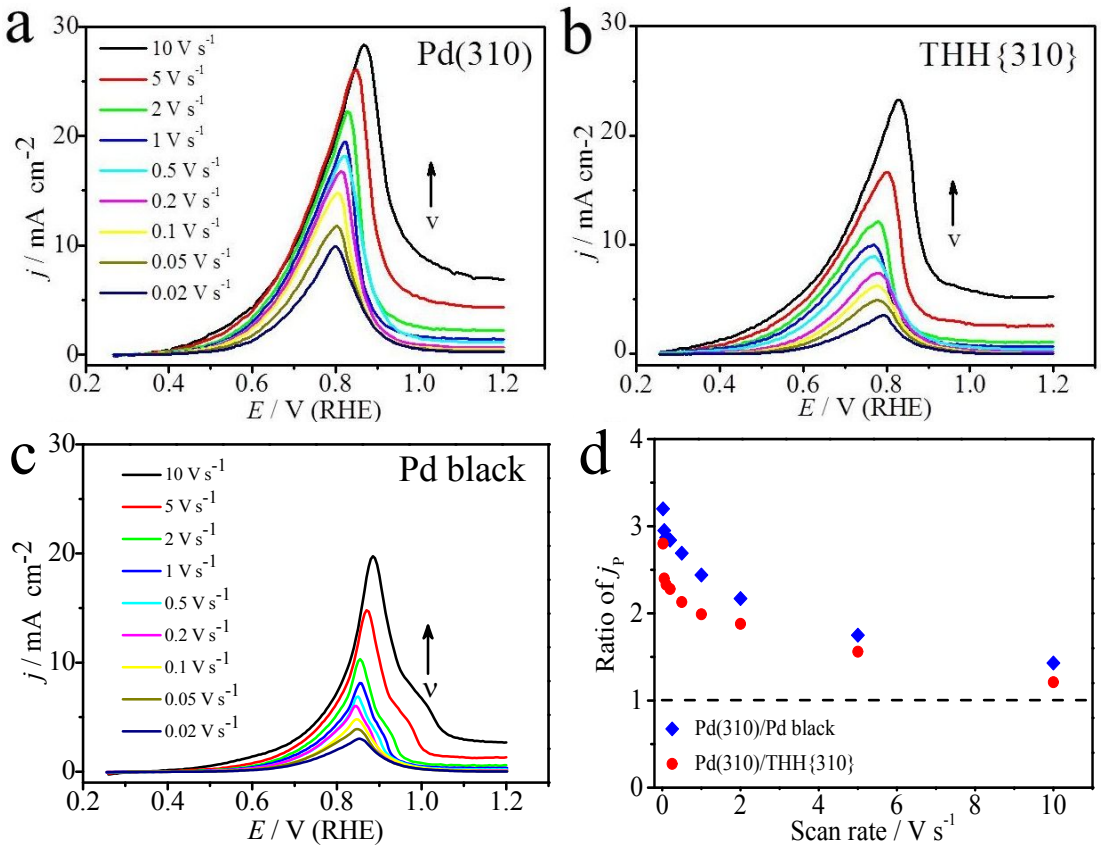

Figure S12. Effect of potential scan rate on the j_p of ethanol oxidation. The forward voltammograms of ethanol oxidation on (**a**) Pd(310), (**b**) THH{310}, and (**c**) commercial Pd black catalyst in 1.0 M CH_3CH_2OH + 1.0 NaOH at different scan rates. **(d)** The ratio of peak current density of Pd(310) to THH{310} and Pd black as a function of potential scan rate.

6. THH{310} Pd NCs with different sizes

The ratio of edge atoms to total surface atoms increases with decreasing particles size. To further understand the role of edge atoms played in catalytic reaction, we synthesized THH Pd NCs of {310} facets with different size. Figure S13a-c show SEM images and size histogram of THH{310} with sizes of 39, 77 and 113 nm. Figure S13d depicts the percentage of edge atoms as a function of particle size. When the size of THH{310} is larger than 80 nm, the ratio of edge atoms to total surface atom is extremely small, less than 1%.

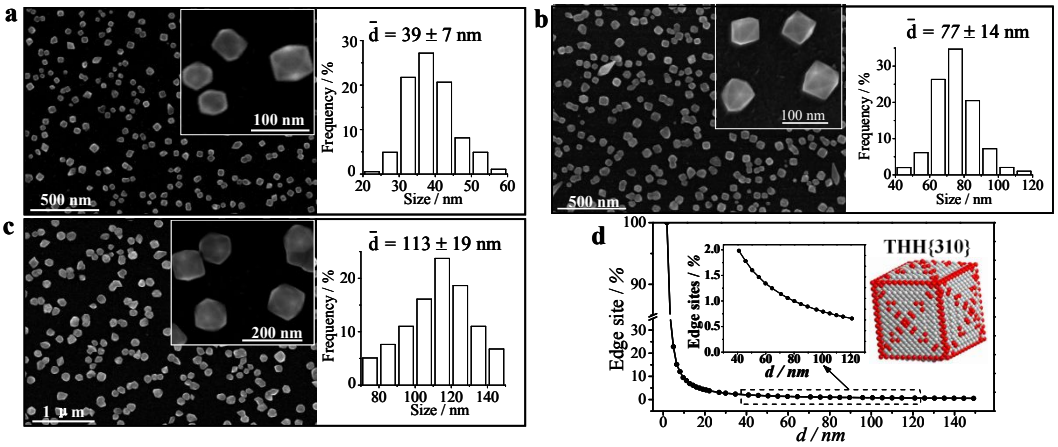

Figure S13. SEM of THH{310} Pd NCs with different sizes and size distribution. THH Pd NCs synthesized at E_N = 0.100 V, t_N = 0.04 s, E_L = 0.600 V, E_U = 1.020 V, f = 100 Hz, in 0.1 mM $PdCl_2$ + 0.1 M $HClO_4$ solution, (**a**) t_{growth} = 15 min; (**b**) t_{growth} = 45 min; (**c**) at E_N = 0.200 V, t_N=0.04 s, E_L =0.600 V, E_U = 1.020 V, f = 100 Hz, t_{growth} = 45 min, and in 0.2 mM $PdCl_2$ + 0.1 M $HClO_4$ solution. (**d**) The ratio of edge atoms to total surface atom on THH{310} with increasing size of THH NCs.